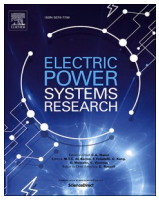
Electric Power Systems Research 262 (2027) 113637



Contents lists available at ScienceDirect

Electric Power Systems Research

journal homepage: www.elsevier.com/locate/epsr



Intelligent control of soft switching solid-state transformer in renewable microgrids using quokka swarm ANN

Pradeep Ammasaikutti [a,*], J Viswanatha Rao [b], M Gnana Sundari [c], B Parvathi Sangeetha [d]

[a] Department of Electrical and Electronics Engineering, Vivekanandha College of Engineering for Women, Namakkal, 637205, TamilNadu, India
[b] Department of Electrical and Electronics Engineering, VNR Vignana Jyothi Institute of Engineering and Technology, Hyderabad, 500090, India
[c] Department of Electrical and Electronics Engineering, Government College of Engineering, Tirunelveli, Tamilnadu, India
[d] Department of Marine Engineering, AMET deemed to be University, Chennai, 603112, Tamilnadu, India

ARTICLE INFO

Keywords:
SS-SST
PV system
DFIG-WECS
BESS
QSO-ANN

ABSTRACT

With the growing adoption of Renewable Energy Sources (RESs), the demand for efficient power management and conversion in microgrids has become crucial. This study presents a Hybrid Renewable Energy System (HRES)-based microgrid integrating Photovoltaic (PV), Doubly Fed Induction Generator (DFIG)-based Wind Energy Conversion System (WECS) and Battery Energy Storage System (BESS). A Soft Switching Solid-State Transformer (SS-SST)-based power conversion architecture is employed to enhance power stability, improve efficiency, and ensures seamless grid integration by contributing voltage regulation and power flow optimization. The Quokka Swarm Optimized Artificial Neural Network (ANN) Controller is implemented for dynamic duty cycle and voltage regulation, ensuring optimal performance under varying load conditions. The Pulse Width Modulation (PWM) generator is tuned using the Quokka Swarm Optimization (QSO) algorithm, significantly improving the control accuracy and reducing power losses. The proposed system is validated through MATLAB simulations and laboratory implementation, demonstrating enhanced voltage regulation and improved power efficiency compared to conventional controllers. The proposed QSO-ANN achieves a settling time of 55 ms, overshoot of $<3\%$, steady-state error below 1% and efficiency up to 97%. The grid current Total Harmonic Distortion (THD) is reduced to below 0.1% in simulation and maintained within 1.5–1.8% in hardware experiments, complying with IEEE-519 standards.

1. Introduction

Resilient, high-performance power electronic infrastructures are becoming more and more imperative as economies throughout the world accelerates towards progressive green energy transformations [1, 2]. Modern microgrids are increasingly incorporating RESs and conventional power topologies are commonly confronted with challenges in coping with load shifts, nonlinear responses and irregular power generations [3]. Because of these restrictions, advanced solutions that combine strong control, high conversion efficiency and flexibility in response to changing operating conditions are required. As flexible and decentralised power distribution networks, microgrids are essential for improving energy accessibility, stability and dependability, especially when powered by HRESs [4,5].However, the intelligence of their control mechanisms and the calibre of the converting devices they interface with have a significant impact on their performance. Low-Frequency Transformers (LFT), which provide isolation and voltage transformation in transmission and distribution, have traditionally served as the foundation of electrical conversion systems. Their bulk, low efficiency at dynamic loads and incapacity to control voltage or attenuate harmonics in the presence of disturbances render them less suitable for the rapidly evolving needs of contemporary grids, despite their robustness and affordability [6–8]. In addition, LFT's enormous physical footprint prevents scalability in small installations and their reactive power and harmonics contribute to grid pollution. Alternative transformer technologies that support high efficiency and sophisticated functions in distributed networks are in high demand as a result of these restrictions [9].In this regard, Solid-State Transformer (SST) have become a revolutionary substitute for LFTs as it replaces bulky electromagnetic cores with high-frequency power electronic converters and medium-frequency transformers.

The working principle of both LFT and SST is illustrated effectively in

* Corresponding author.
E-mail address: apradeepdr@gmail.com (P. Ammasaikutti).

https://doi.org/10.1016/j.epsr.2026.113637
Received 11 April 2026; Received in revised form 13 June 2026; Accepted 23 June 2026
Available online 2 July 2026
0378-7796/© 2026 Elsevier B.V. All rights are reserved, including those for text and data mining, AI training, and similar technologies.

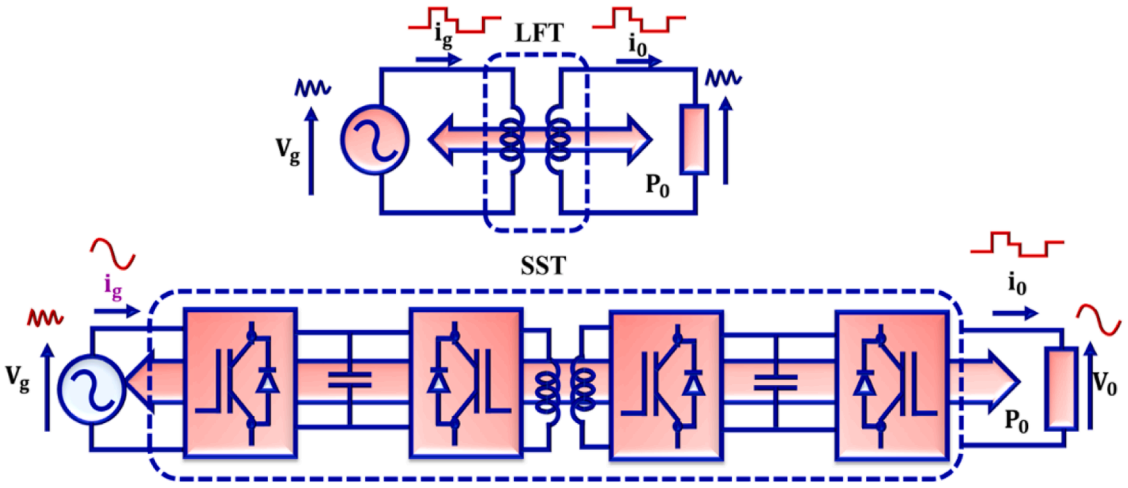


Fig. 1. Working principle of both LFT and SST.

Fig. 1. According to studies, SST increases efficiency by a number of percentage points and decrease transformer volume by >60%, which renders them ideal for applications requiring high power density and compactness [10]. Beyond simple voltage conversion, SST enable bi-directional power flow, provide harmonic mitigation, regulate voltage under disturbances and facilitate the direct integration of RESs and distributed storage devices.They are therefore essential for the future generation of microgrids that rely on RESs and smart grids. On taking into account that SST is modular, their benefits are further enhanced [11]. SST architecture is divided into single, two, or three-stage versions based on the needs of the application. Usually, each stage supports both AC and DC grid linkages at different voltage levels by integrating DC-DC, DC-AC or AC-DC converters with high-frequency isolation. For instance, three-stage SST provides better controllability at the expense of increased complexity, but two-stage SST with a High-Voltage DC (HVDC) link are especially effective in long-distance transmission. SST versatility across a range of industries is demonstrated by their adaptable configurations, which enable them to be customised for high-power traction systems, offshore renewable integration and Electric Vehicle (EV) fast-charging stations [12]. Among this range of technologies, the Soft Switching-SST (SS-SST) has attracted particular attention. Resonant and leakage-inductance-based methods are used by SS-SST to enable soft switching, which lowers Electromagnetic Interference (EMI), supports higher operating frequencies and minimises switching losses. SS-SST provide increased efficiency, reduced thermal stress and higher reliability in addition to galvanic isolation and voltage transformation. These characteristics make them ideal for integration with sensitive storage devices and intermittent RESs. Due to these characteristics, SS-SST is positioned as a key technology for overcoming the intrinsic drawbacks of hard-switching SST and traditional LFT [13,14].

Adopting SS-SST alone, however, is insufficient as control measures are essential to maximising its potential. In renewable microgrids, where environmental variables continuously impact energy generation and consumption, the requirement for strong, intelligent control is particularly vital.The power generated by sources in microgrids is generally nonlinear and intermittent owing to variations which in turn affect the power flow, stability and harmonic performance. Degradation in dynamic response may occur due to the absence of appropriate controllers and hence there is a need for advanced control measures aiding in the dynamic regulation of duty cycles. The most popular option among the extensively researched control strategies is the Proportional-Integral (PI) controller, which is preferred for its accessibility, simplicity and efficient steady-state error elimination capability [15]. However, PI controllers are insufficient for variable renewable conditions since they are extremely sensitive to parameter changes and show poor dynamic response under nonlinear disturbances [16]. By improving harmonic compensation and removing steady-state error in AC tracking applications, Proportional-Resonant (PR) controllers subdue certain limitations. However, they need the resonance frequency to be carefully adjusted, and when frequency deviations happen, they are prone to losing stability [17]. Because Sliding Mode Control (SMC) is resilient to changes in parameters and external disturbances, it has been widely used in SST [18]. Although this method guarantees strong immunity to parameter variations and offers swift transient response, the persistent issue of chattering leads to elevated switching stress and power losses, making it less suitable for high-frequency SS-SST applications. Another advanced option is Model Predictive Control (MPC) [19], which offers predictive optimisation over a finite horizon and multivariable handling. Different types of MPC techniques including Finite Control Set MPC (FCS-MPC) [20], Continuous Control Set MPC (CCS-MPC) [21] and Three Vector MPC (TV-MPC) [22] have been implemented for the control of SST. Even though MPC performs well in terms of handling constraints and quick transient recovery, its large computing load makes real-time implementation difficult in high-switching-frequency settings. Intelligent and soft computing-based techniques have also gained traction in recent years.Fuzzy logic control (FLC) effectively handles nonlinearities and uncertainties in SS-SST by enabling rule-based decision making without the need for an exact mathematical model [23]. Fuzzy rules are heuristic in nature and their efficacy is highly dependent on expert knowledge, which restricts generalisation. With the ability to learn and approximate nonlinear dynamic interactions, ANN controllers are another excellent option [24]. Although conventional ANN is resilient and flexible, they frequently overfit, need huge training datasets and lack global optimisation, which results in less-than-ideal duty cycle management. Linear Quadratic Regulator (LQR) controller [25] has been explored for multi-stage SST and it achieves smooth control action and stability, but struggle under strong nonlinearities or parameter uncertainties common in renewable microgrids.

In [26], ANN is used for SST-based systems providing rapid decision-making along with robust ability of nonlinear mapping. This approach offers protective applications and is much versatile in nature, but requires extensive offline tuning due to the dependency on statistical features and decomposition levels. Moreover, overfitting and generalization issues persist, which could be tackled only by relying on a large and representative training dataset. The incorporation of ANN for harmonic compensation in SST [27] facilitates robust nonlinear mapping and adaptive filtering ability aiding in improving harmonic suppression and inheriting expert knowledge. With this approach, robustness against load variations is attained, but the adopting of numerous compensators

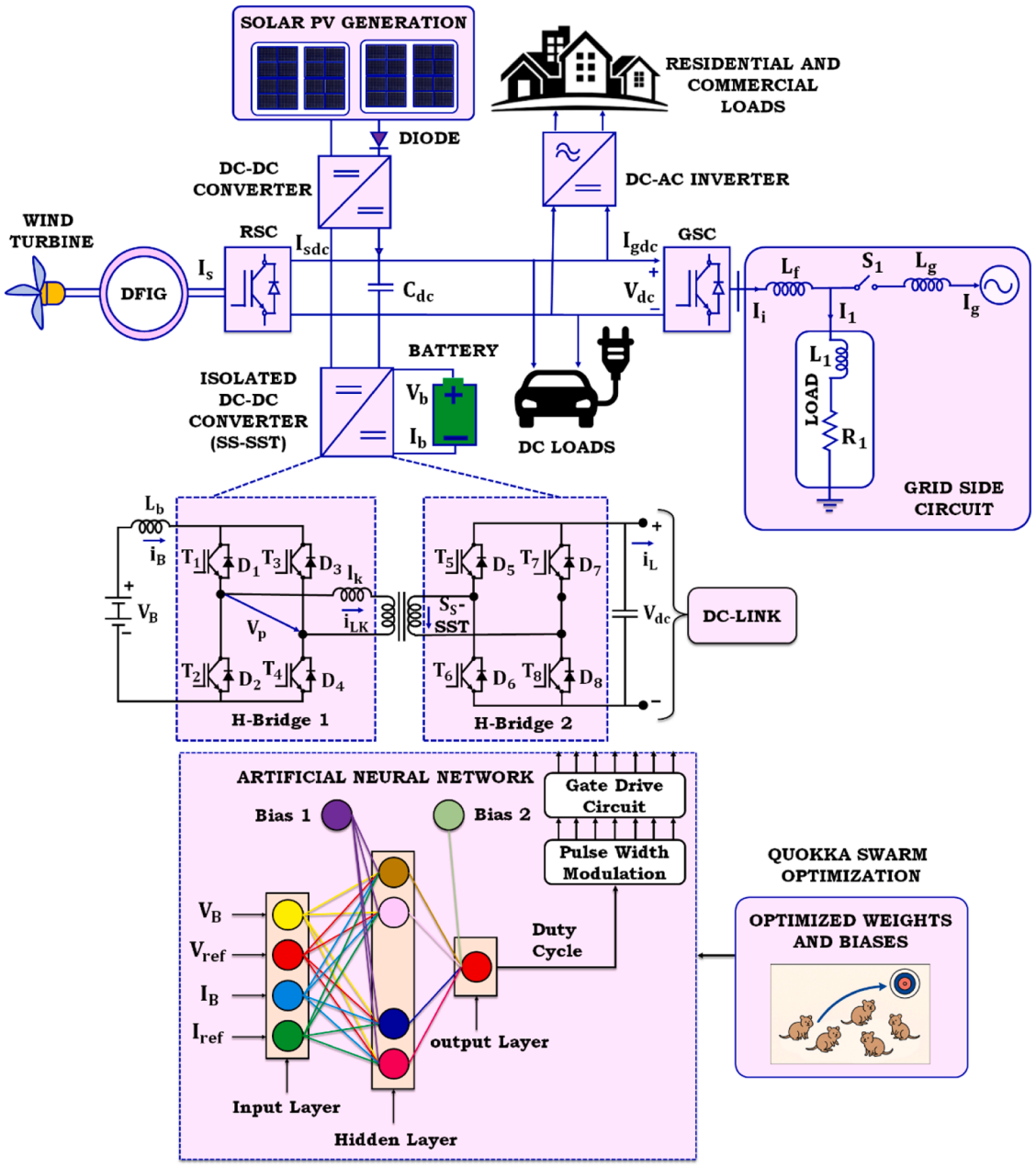


Fig. 2. QSO-ANN controlled SS-SST integrated hybrid renewable microgrid architecture.

leads to high control complexity complicating implementation. Moreover, this approach requires offline efforts and substantial expert intervention. In [28], ANN with SST-based architecture is proposed in which ANN offers enhanced nonlinear control ability along with regulation of voltage efficiently. However, certain limitations including lack of adaptability under unseen operating scenarios without online learning exists.

Based on the above discussion, a clear research gap exists in the integration of SS-SSTs with intelligent control approaches for microgrids based on HRES under nonlinear scenarios. In spite of superior efficiency and improved power quality offered by SS-SSTs, their performance highly relies on adopted control concept. Traditional controllers lack robustness against renewable intermittency and parameter variations whereas advanced approaches suffer from excessive computational burden and chattering effects at high switching frequencies. Moreover, intelligent controllers remain constrained due to overfitting issues and lack of global optimization along with suboptimal duty cycle regulation. This demands the introduction of a globally optimized and intelligent control framework for assuring fast dynamic response and improved voltage regulation.

To overcome the drawbacks of existing control methods, a novel QSO-ANN controller is proposed in this work for the control of SS-SST. Fig. 2 provides the architecture of PV-Wind-Battery microgrid regulated by QSO-ANN controlled SS-SST. The major contributions of this work are,

- Development of a hybrid renewable microgrid model integrating PV, wind and battery energy storage for stable and efficient power management.
- Adoption of SS-SST as the central conversion unit to achieve high-frequency isolation, reduced switching losses and improved reliability.

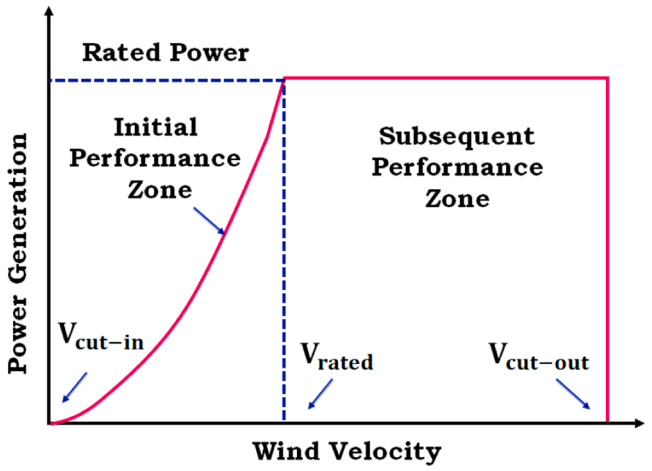


Fig. 3. Performance zones of a WT based on wind speed.

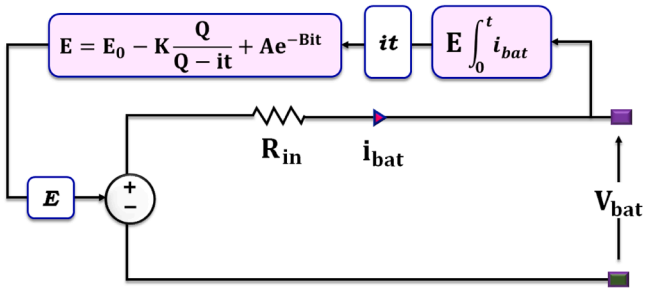


Fig. 4. Mathematical representation of battery dynamics.

- Design of an intelligent QSO-ANN controller, combining the nonlinear learning strength of ANN with the global optimization ability of QSO algorithm.
- Dynamic duty cycle regulation of the SS-SST, ensuring robust voltage and current stability under varying load and generation conditions.
- Enhanced performance compared to conventional controllers, demonstrated through MATLAB simulations in terms of reduced steady-state error, minimized overshoot, faster settling time and improved efficiency.

2. System modelling

2.1. Modelling of PV array

Numerous mathematical models, from intricate semiconductor-based formulations to basic empirical formulae, can be used to estimate the power production from PV panels. This study uses a computationally efficient model that links the two main variables of incident solar irradiance and cell operating temperature to PV power generation. The instantaneous PV power output is expressed as,

$$P_{PV_{out}}(t) = P_{PV_{ref}} \times \frac{G_t(t)}{G_{t_{ref}}} \times \left[1 + K_T\left(T_C(t) - T_{C_{ref}}\right)\right] \quad (1)$$

Here, the actual PV power output and rated power of single PV module are represented using the terms $P_{PV_{out}}(t)$and $P_{PV_{ref}}$, respectively. The term $G_t(t)$ specifies the instantaneous solar irradiance incident on the panel surface and the term K_T is the temperature coefficient of maximum power. The terms $T_C(t)$ and $T_{C_{ref}}$ specifies the actual and reference cell temperatures, respectively. Moreover, the terms representing the Standard Test Conditions (STC) are $G_{t_{ref}} = 1000W/m^2$and $T_{C_{ref}} = 25^{\circ}C$. The cell temperature is calculated as a function of the surrounding temperature and irradiance rather than being directly measured in real time.An empirical relationship that is commonly acknowledged is,

$$T_C(t) = T_{amb}(t) + \beta \cdot G_t(t) \quad (2)$$

Here, $T_{amb}(t)$ is the ambient air temperature ($^{\circ}$C) and β is the thermal coefficient that captures irradiance-induced heating. For crystalline silicon modules, $\beta \approx 0.0256^{\circ}C \cdot m^2/W$. When the formula is applied to a PV array with several modules, the total power output is estimated as,

$$P_{array}(t) = P_{PV_{out}}(t) \times N_{PV} \times \eta_{PV} \quad (3)$$

Where, N_{PV} is the total count of PV modules connected in the microgrid system and η_{PV} is the total conversion efficiency accounting for wiring, dust, mismatch and partial shading losses.

2.2. Modelling of wind turbine

A wind turbine's (WT) output power is intrinsically reliant on the incident wind speed, which varies greatly with altitude and local topography. A vertical wind profile model is needed to determine the wind speed at a turbine's hub height. The relationship between wind velocity and power output in WT is provided in Fig. 3. The power-law profile is used in this work and is given as,

$$V(h) = V_{ref} \times \left(\frac{h}{h_{ref}}\right)^{\alpha} \quad (4)$$

Where, the term $V(h)$ specifies the wind velocity at hub height h, the term V_{ref} is the measured wind speed at the reference height h_{ref} and the term α is the wind shear exponent. Three essential wind speeds characterise the operational regimes in which a WT's nonlinear conversion of wind kinetic energy into electrical power occurs. These wind speeds are cut-in speed (V_{cut-in}), rated speed (V_{rated}) and cut-out speed ($V_{cut-out}$). The instantaneous power extracted from WT is expressed as,

$$P_{wt}(t) = \begin{cases} 0, & V < V_{cut-in} \\ P_r\left(\dfrac{V^3 - V_{cut-in}^3}{V_{rated}^3 - V_{cut-in}^3}\right), & V_{cut-in} \le V < V_{rated} \\ P_r, & V_{rated} \le V \le V_{cut-out} \\ 0, & V > V_{cut-out} \end{cases} \quad (5)$$

Where, the rated output power is specified as P_r. The combined power of several turbines in a wind energy system is calculated by,

$$P_{farm}(t) = P_{wt}(t) \times N_{wt} \times \eta_{wt} \quad (6)$$

Where, the total deployed turbine count is specified as N_{wt} and combined efficiency factor is specified as η_{wt}. The integration of WT into the hybrid renewable microgrid is accomplished using DFIG in this work, which guarantees variable-speed operation, heightened efficiency and flexible power regulation.

2.3. Modelling of battery

Battery Energy Storage Systems (BESS) are essential for resolving the imbalance between energy supply and demand, especially in microgrids that are fuelled by sporadic RESs [29]. Because renewable energy outputs are subject to weather and environmental fluctuations, BESS provides stability by storing extra energy during periods of high generation and releasing it when generation is insufficient. Due to this, batteries are essential for modern smart grid's ability to be dependable and resilient. The discharge characteristics of battery is modelled using Shepherd model illustrated in Fig. 4. For precisely depicting a battery's nonlinear discharge profile, the model takes into account the impacts of internal resistance, polarisation processes and exponential voltage dynamics.

The expression for the governing electrical relationships is,

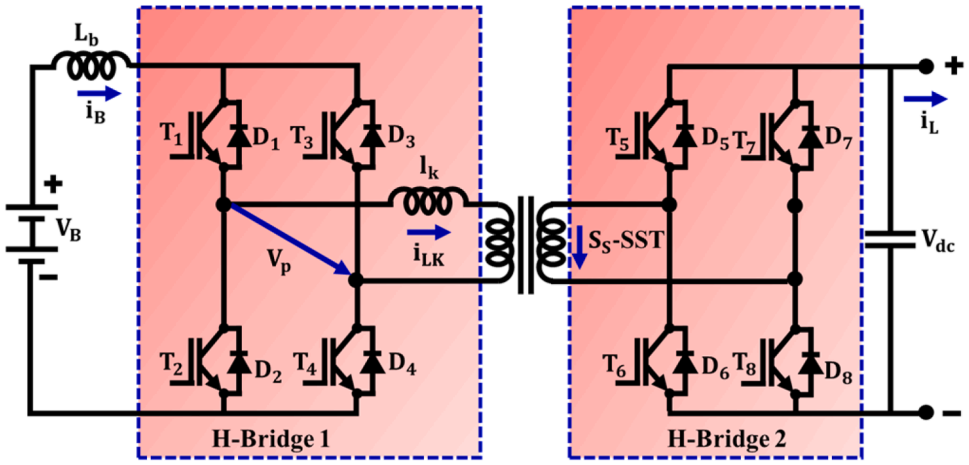


Fig. 5. Equivalent circuit of SS-SST for battery interfacing.

$$V_B = E - R_{in} \cdot i_B \tag{7}$$

$$E = E_0 - K\frac{Q}{Q - it} + Ae^{-Bit} \tag{8}$$

In the above equations, the exponential capacity is specified as B, the exponential voltage is specified as A, the battery capacity is specified a Q, the polarization constant is specified as K, the internal resistance is specified as R_{in} and battery constant voltage is specified as E_0.

2.4. Modelling of soft-switching solid-state transformer (SS-SST)

The SS-SST is an advanced transformer technology thatutilizes solid-state semiconductor components to improve the reliability of power conversion systems. In contrast to conventional transformers that depend on large mechanical and electromagnetic components, the SS-SST uses semiconductor switches integrated into modular H-bridge converter architectures. This configuration significantly improves efficiency, makes maintenance simpler and significantly lowers size and weight.The prominent feature of SS-SST is the soft-switching operation which in turn reduces switching losses and EMI. The medium-frequency transformer offers voltage scaling and galvanic isolation thereby aiding in high power density and compact design with the reduction of size and weight. Also, rapid dynamic regulation of voltage and bidirectional power flow is aided with the help of the modular dual H-bridge architecture. Moreover, with the adopting of soft-switching mechanism, improved reliability and thermal performance are attained. Two H-bridge converters coupled by a medium-frequency transformer make up the core topology of the SS-SST configuration illustrated in Fig. 5. The primary H-bridge converter (H-bridge 1) is in charge of transforming input battery voltage into a high-frequency AC waveform. The generated AC is coupled through a medium-frequency transformer, offering galvanic isolation, voltage transformation, and leakage inductance effects for soft-switching functionality. Depending on the intermediate transformer's turns ratio, the secondary H-bridge converter (H-bridge 2) then transforms the high-frequency AC voltage back into DC voltage to the desired voltage level. The DC source and input inductor dynamics of SS-SST is expressed as,

$$V_B = L_b\frac{di_B}{dt} + v_p \tag{9}$$

Where, V_B is the input battery voltage, L_b is the input inductor, L_B is the input current and v_p is the primary side transformer voltage. The primary transformer voltage is expressed by the switching states of the primary-side H-bridge,

$$v_p = (S_1S_4 - S_2S_3)V_B \tag{10}$$

Where, S_1, S_2, S_3, S_4 are the switching states of switches T_1, T_2, T_3, T_4, respectively.

The transformer is modelled by including the leakage inductance (L_{lk}) and the magnetizing inductance (L_m). The primary and secondary voltages are expressed as,

$$v_p = L_{lk}\frac{di_{L_{lk}}}{dt} + n \cdot v_s \tag{11}$$

$$v_s = \frac{1}{n}\left(v_p - L_{lk}\frac{di_{L_{lk}}}{dt}\right) \tag{12}$$

Where, v_s is secondary-side voltage, $i_{L_{lk}}$ is the leakage inductance current and n is the transformer turns ratio. The relationship between primary and secondary currents through the transformer is given by,

$$i_{L_{lk}}(t) = i_p(t) - i_m(t) \tag{13}$$

$$i_m(t) = \frac{1}{L_m}\int v_p(t)dt = \frac{1}{L_m}\int\left[(S_1S_4 - S_2S_3)V_B - L_{lk}\frac{di_{L_{lk}}}{dt}\right]dt \tag{14}$$

The secondary current in relation to primary leakage inductance current is expressed as,

$$i_s(t) = \frac{i_{L_{lk}}(t)}{n} = \frac{1}{n}\left[i_p(t) - i_m(t)\right] \tag{15}$$

The dynamic behaviour of the DC-link capacitor voltage (V_{dc}) on the secondary side is described by a nonlinear differential equation, linking secondary transformer current (i_s) and load current (i_L),

$$C_{dc}\frac{dV_{dc}(t)}{dt} = \frac{(S_5S_8 - S_6S_7)}{n}\left[i_p(t) - \frac{1}{L_m}\int\left\{(S_1S_4 - S_2S_3) - L_{lk}\frac{di_{L_{lk}}}{dt}\right\}dt\right] - i_L(t) \tag{16}$$

Incorporating nonlinear transformer magnetizing and leakage inductance effects, the relationship for the leakage inductance current is expressed as,

$$\frac{di_{L_{lk}}(t)}{dt} = \frac{1}{L_{lk}}\left[(S_1S_4 - S_2S_3)V_B - n(S_5S_8 - S_6S_7)V_{dc}\right] \tag{17}$$

Load voltage and current relationships, factoring in impedance (Z_L) are expressed as,

$$V_{load}(t) = m(t) \cdot V_{dc}(t); i_L(t) = \frac{m(t) \cdot V_{dc}(t)}{Z_L} \tag{18}$$

Where the modulation index $m(t)$ represents the complex modulation derived from the optimal duty cycle and switching angle, mathemati-

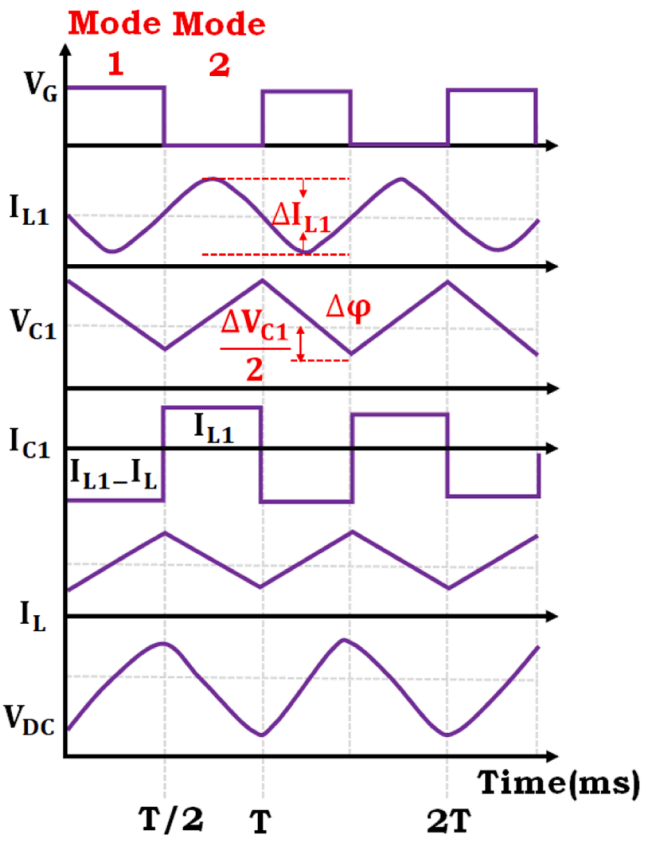


Fig. 6. Operational waveform of SS-SST.

cally represented as,

$$m(t) = \sum_{j=1}^{M} \delta_j \cdot sin(\omega_s t + \alpha_j) \tag{19}$$

Here, δ_j and α_j are optimized switching angles and duty cycle parameters, ω_s is the switching angular frequency and M represents the number of switching transitions considered per cycle. Fig. 6 provides the switching waveform of SS-SST. The SS-SST is controlled by QSO-ANN technique, in which QSO optimises ANN parameters to produce stable voltage regulation, lower switching losses and increased efficiency.

2.5. Quokka swarm optimized artificial neural network (QSO-ANN) controller

To ensure stability and effective energy management, the adoption of intelligent control techniques is indispensable in microgrids powered by RESs. Hence, the integration of bio-inspired optimization algorithms with machine learning models has gained significant traction in recent times. The QSO-ANN controller, which is employed for the control of battery, is an advanced control strategy combining the learning capability of ANN with the global optimization power of QSO. It specifically regulates the functioning of SS-SST, which is interfaced with BESS. The purpose of the QSO-ANN controller is to produce duty cycles in real time

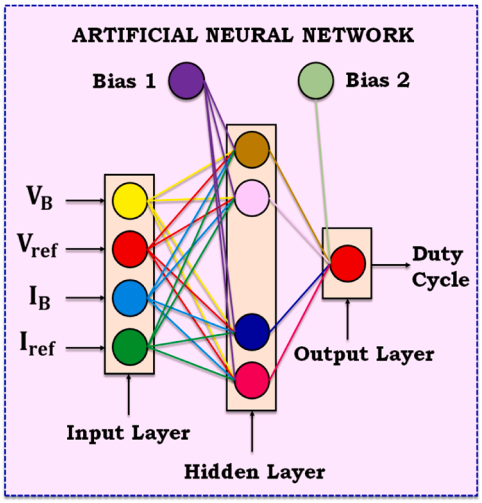


Fig. 8. Structure of ANN.

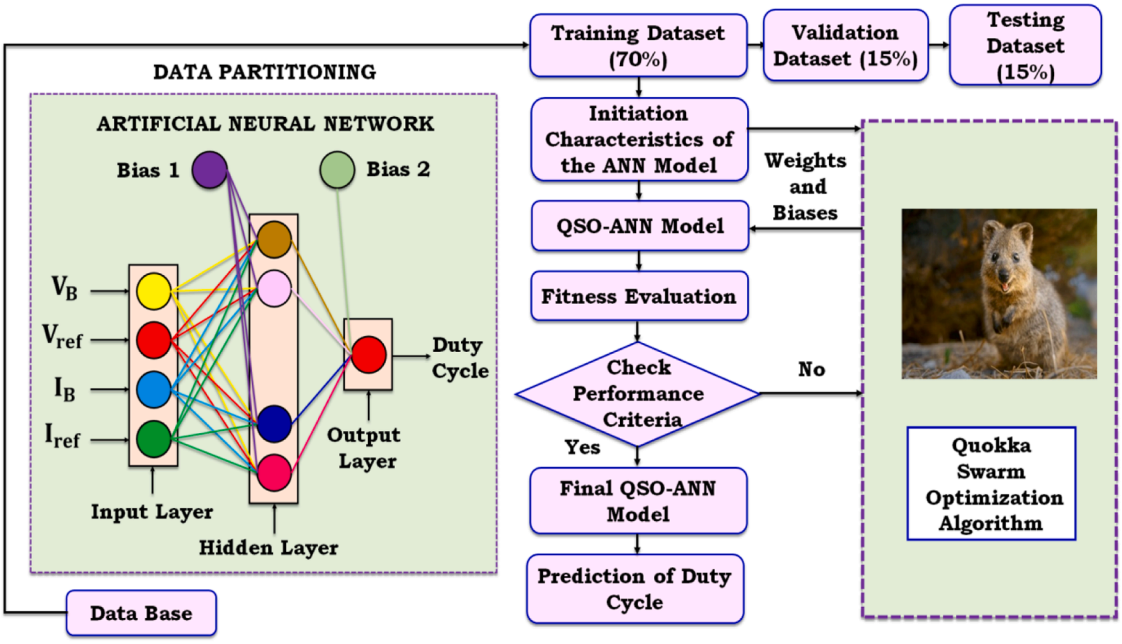


Fig. 7. Structure of QSO-ANN controller.

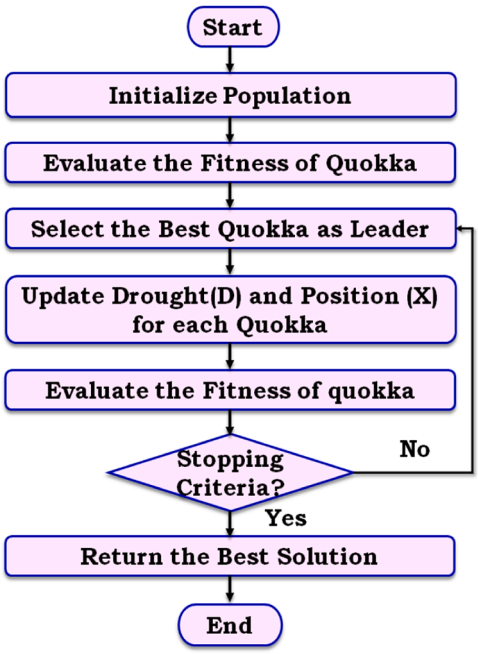


Fig. 9. Flowchart of QSO algorithm.

Table 1
Parameter specifications of QSO-ANN controller.

Category	Parameter	Specification
ANN	Input layer neurons	4
	Hidden layer neurons	15
	Output neuron	1
	Activation function (Hidden layer)	Sigmoid
	Activation function (Output layer)	Linear
	Learning Objective	Minimize quadratic error between V_{ref}, I_{ref} and V_B, I_B
QSO	Population size (N)	50 quokkas
	Maximum iterations	100
	Drought coefficient range (D)	[0,1]
	Temperature factor (T)	[0.20]
	Humidity factor (H)	[0.30]
	Nitrogen factor (N)	[0,1]
Control Objectives	Voltage tracking weight (α)	0.6
	Current tracking weight (β)	0.2
	Duty cycle range (D)	[0,1]
	Output target	Stable V_{dc} and I_{dc} with minimal

that regulate the switching function of SS-SST.The objective of the controller is to minimise power losses and improve system efficiency while maintaining a steady output voltage and current from the battery through the transformer. Fig. 7 provides the structure of QSO-ANN controller. The ANN controller is trained precisely to forecast the necessary duty cycle using input parameters like reference and actual battery voltages and currents. The QSO algorithm is used to train and fine-tune the ANN in order to guarantee peak performance in variable operating environments.

2.5.1. ANN controller

ANN provides a strong substitute for conventional linear controllers in the context of intelligent control for nonlinear, time-varying power conversion systems like SS-SST. The dataset used for training the ANN controller was generated from extensive simulations under diverse operating conditions, including variations in solar irradiance, wind speed, battery state-of-charge, load demand and grid-side disturbances. The samples were collected at a fixed sampling interval corresponding to the controller execution period to adequately capture both steady-state and transient system dynamics. Each sample consisted of the input feature vector and the corresponding optimal duty-cycle target. The target duty-cycle labels were obtained from the control actions generated by a well-tuned reference controller and subsequently refined through iterative QSO optimization to minimize the composite voltage-current tracking error. Prior to training, all input and output variables were normalized to the range [0,1] using min-max scaling to improve convergence and prevent numerical bias caused by differing variable magnitudes. The data for ANN is partitioned into 70% for training, 15% for testing and 15% for validation. The proposed ANN controller as in Fig. 8, learns and approximates the nonlinear dynamic behaviour of the battery-fed SS-SST in the HRES, allowing it to simultaneously control both voltage and current. A fully connected feedforward Multilayer Perceptron (MLP) makes up the ANN model. The input layer receives real-time error signals, and the output layer provides the PWM module controlling the SS-SST's H-bridge switching network with the necessary duty cycle instruction. The input to the ANN controller consists of a vector $X(t)\epsilon\mathbb{R}^4$, composed of instantaneous error signals and their respective rates of change, such that,

$$X(t)=\begin{bmatrix} e_v(t) \\ \Delta e_v(t) \\ e_i(t) \\ \Delta e_i(t) \end{bmatrix}=\begin{bmatrix} V_{ref}(t)-V_B(t) \\ \frac{d}{dt}\left[V_{ref}(t)-V_B(t)\right] \\ I_{ref}(t)-I_B(t) \\ \frac{d}{dt}\left[I_{ref}(t)-I_B(t)\right] \end{bmatrix} \tag{20}$$

Where, V_{ref} and I_{ref} denote the reference output voltage and current and V_B and I_B represent the actual battery-side voltage and current measurements, respectively.

The ideal control signal is generated using these inputs, which capture the SS-SST's dynamic state. The hidden layer computation begins with a linear transformation of the input vector using a weight matrix $W^{(1)}\epsilon\mathbb{R}^{n_h\times 4}$ and a bias vector $b^{(1)}\epsilon\mathbb{R}^{n_h}$. For the j-th hidden neuron, the net input is given by,

$$z_j(t)=\sum_{i=1}^{4}\omega_{ji}^{(1)}X_i(t)+b_j^{(1)} \tag{21}$$

This net input is then passed through a nonlinear activation function, which is a sigmoid function $\sigma(x)=\frac{1}{1+e^{-x}}$, yielding the hidden layer output,

$$h_j(t)=\sigma\left(z_j(t)\right)=\frac{1}{1+exp\left(-\sum_{i=1}^{4}\omega_{ji}^{(1)}X_i(t)-b_j^{(1)}\right)}\ \forall j\in\{1,2,\ldots,n_h\} \tag{22}$$

The output layer receives the vector $H(t)=\left[h_1(t),h_2(t),\ldots,h_{n_h}(t)\right]^T$ and performs another affine transformation using weight matrix $W^{(2)}\epsilon\mathbb{R}^{1\times n_h}$and $b^{(1)}\epsilon\mathbb{R}$. The scalar control signal $u(t)$, which represents the optimal duty cycle, is given by,

$$u(t)=f_o\left(\sum_{j=1}^{n_h}\omega_j^{(2)}h_j(t)+b^{(2)}\right) \tag{23}$$

Where, $f_o(x)$ is a linear or saturated linear function depending on the desired control range $D\epsilon[0,1]$. Hence, the ANN is compactly represented as a composite function,

$$u(t)=f_{ANN}(X(t))=W^{(2)}\cdot\sigma\left(W^{(1)}\cdot X(t)+b^{(1)}\right)+b^{(2)} \tag{24}$$

Algorithm 1
Pseudocode of QSO-ANN.

```
Input: Reference signals V_ref(t), I_ref(t)
Measured signals V_B(t), I_B(t)
Population size N, maximum iterations Tmax
ANN structure (input layer, hidden neurons, output neuron)
Output: Optimal ANN weights and biases {W*, b*}
Control signal u(t) → Duty cycle for PWM of SS − SST
Begin
1. Initialize ANN parameters (weights W, biases b) randomly.
2. Initialize QSO population:
For each quokka i in {1, ..., N}
Assign candidate ANN parameter set Xi = {Wi, bi}
EndFor
3. For iteration = 1 to Tmax do:
a) For each quokka i:
− Feed input vector X(t) = [ev, Δev, ei, Δei]
− Evaluate ANN output u(t) = fANN(X(t), Wi, bi)
− Compute fitness Fi using loss function:
Fi = (1/T) ∫ 0^T [ α(V_ref − V_B)^2 + β(I_ref − I_B)^2 ] dt
EndFor
b) Identify leader quokka (best solution with minimum Fi).
c) For each quokka i:
− Update drought coefficient:
D_new = (T + H) / (0.8 * D_old) + Δw * rand * ΔX − Update position (weights and biases):
Xi_new = Xi_old + D_new * N
EndFor
d) Replace old population with new population.
e) Check convergence criteria (fitness threshold or iteration limit).
4. EndFor
5. Set optimized ANN parameters:
{W*, b*} = parameters of leader quokka
6. Real − time ANN inference:
− With optimized {W*, b*}, compute duty cycle u(t) = fANN(X(t))
− Apply u(t) to PWM module controlling SS − SST.
End
```

Table 2
Parameter specification of the HRES.

PV system			
Attributes	Values	Attributes	Values
Number of Parallel Strings	120	Series modules per string	9
Short-Circuit Current	5.17A	Open Circuit Voltage	43.99 V
Voltage at Maximum Power	36.6 V	Current at Maximum Power	4.78 A
Maximum power of module	175.09W	Diode Ideality factor	0.988
DC-DC Converter			
Switching frequency	10kHz	L, C	1mH, 100μF
DFIG based WECS			
Number of Wind Turbines	4	Stator Resistance	0.023 Ω (pu)
Stator Inductance	0.18mH (pu)	Rotor Inductance	0.16mH(pu)
Rotor Resistance	0.016Ω (pu)	Magnetizing Inductance	2.9mH
Inertia Constant	0.685Hs	Pairs of Poles	3
Battery			
Number of battery units	10	Ratings	100Ah, 42V
SS-SST			
Transformer count	17	Number of primary turns	31
Transformer area product	25.12m^4	Number of secondary turns	425
Winding height of transformer	0.183m	Winding width of transformer	0.145m
Clearance width of winding	0.003m	Diameter of transformer core circle	0.45m

The output $u(t)$ is directly applied to the PWM module that controls the duty cycle of the SS-SST's primary H-bridge inverter. This allows the SS-SST to regulate the output voltage and current, thereby stabilizing the downstream DC bus or grid interface. The learning phase of the ANN involves optimizing the weights $W^{(1)}, W^{(2)}$ and biases $b^{(1)}, b^{(2)}$ using QSO. The optimization seeks to minimize the time-averaged quadratic error between the reference and actual output variables. The composite loss function $\mathscr{L}$ is defined over a finite time horizon T as,

$$\mathscr{L} = \frac{1}{T}\int_0^T \left[\alpha\left(V_{ref}(t) - V_B(t)\right)^2 + \beta\left(I_{ref}(t) - I_B(t)\right)^2\right]dt \tag{25}$$

Where, α and β are scalar weighting factors that prioritize voltage and current control objectives, respectively. The optimization problem becomes,

$$\min_{W^{(1)}, W^{(2)}, b^{(1)}, b^{(2)}} \mathscr{L} \tag{26}$$

During the training phase, the QSO algorithm generates a population of candidate weight-bias configurations and iteratively refines them based on the swarm's fitness function. The ANN weights and biases were initially randomized within a small uniform range and QSO was employed offline to optimize these parameters by minimizing the loss function over the training dataset. The optimization process was terminated when either the maximum number of iterations was reached or the improvement in fitness value fell below a predefined tolerance threshold. The finalized ANN parameters were then embedded into the real-time controller, where the trained network directly generated duty-cycle commands for the PWM module based on instantaneous voltage and current error signals. Thus, QSO optimization is performed offline during the training phase, while the ANN executes online in real time, ensuring both computational efficiency and rapid control response during practical operation.

2.5.2. Quokka swarm optimization (QSO) algorithm

QSO is used to efficiently train the ANN and allow it to adjust to the complex, nonlinear, and dynamic behaviour of the SS-SST system under various operating situations. QSO is opted in this work due to its balanced ability, low computational complexity and fast convergence. Traditional algorithms face extensive tuning of parameters and premature convergence whereas QSO employs adaptive swarm behaviours which in turn enables improved global search with solution diversity. When compared to bio-inspired algorithms, QSO demonstrates enhanced robustness and exhibits stable convergence even under nonlinear circumstances. The control parameters required by QSO is less which in turn makes it highly appropriate for high switching frequency applications. The feeding, hydration, and thermoregulation habits of quokkas, a tiny marsupial native to Western Australia, serve as the model for the QSO algorithm [30]. The position update mechanism in

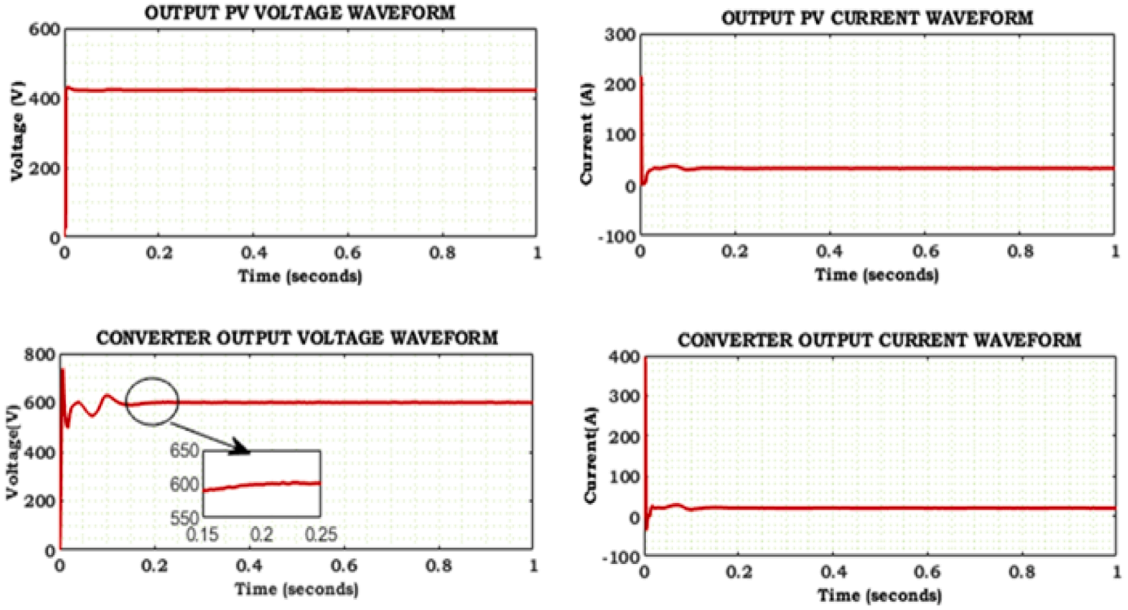


Fig. 10. Operational characteristics of PV system under constant operating conditions.

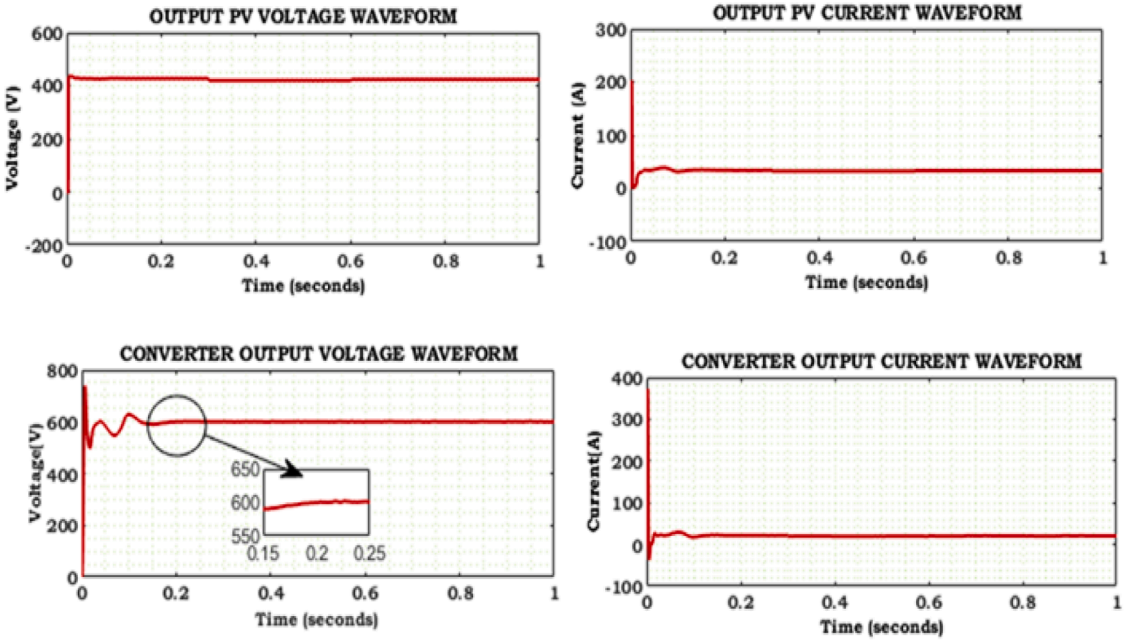


Fig. 11. Operational characteristics of PV system under variable operating conditions.

the optimisation space is defined by mathematically abstracting quokka's natural behaviours, which include leader-following behaviour in groups, social interaction and adaptive foraging under environmental constraints (temperature, humidityand nitrogen availability). In the procedure, each quokka stands for a potential ANN weight vector solution that searches the solution space for the global optimum that reduces the error in tracking voltage and current.

In QSO, the optimization begins with the random initialization of a population of quokkas. The movement of each quokka through the solution space is governed by two primary update equations. The first equation defines the updated drought factor D^{new}, which modulates the quokka's tendency to explore or exploit,

$$D^{new} = \frac{(T+H)}{(0.8 \times D^{old})} + \Delta w \times rand \times \Delta X \tag{27}$$

Here, $T\epsilon[0.2, 0.44]$ and $H\epsilon[0.3, 0.65]$ represent the environmental parameters of temperature and humidity, which are used metaphorically to define the adaptive pressure or stress on the system. $D^{old}\epsilon[0,1]$is the previous drought coefficient controlling memory-based inertia. $\Delta w = w_{leader} - w_i$is the fitness differential between the best-performing ANN configuration and the current quokka's ANN parameters. $\Delta X = X_{leader} - X_i$represents the Euclidean distance in parameter space $rand\epsilon[0,1]$ is a uniformly distributed random number introducing exploration.

Once the drought coefficient is updated, the new position for the i-th quokka, which is the updated ANN weight is expressed as,

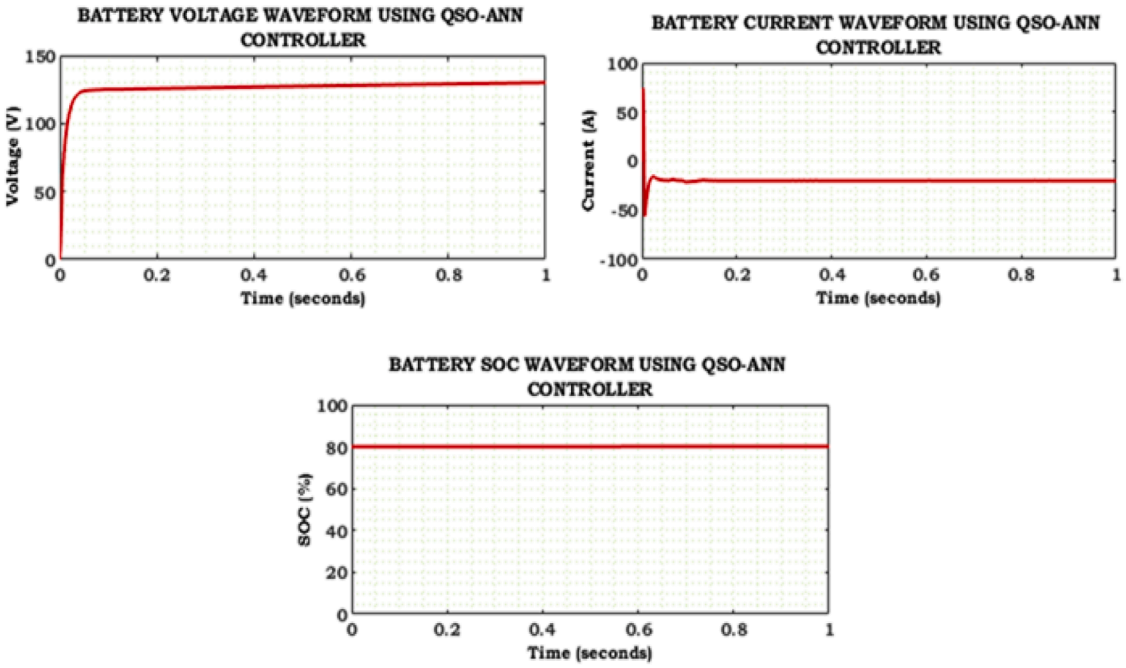


Fig. 12. Battery performance characteristics under QSO-ANN controlled SS-SST.

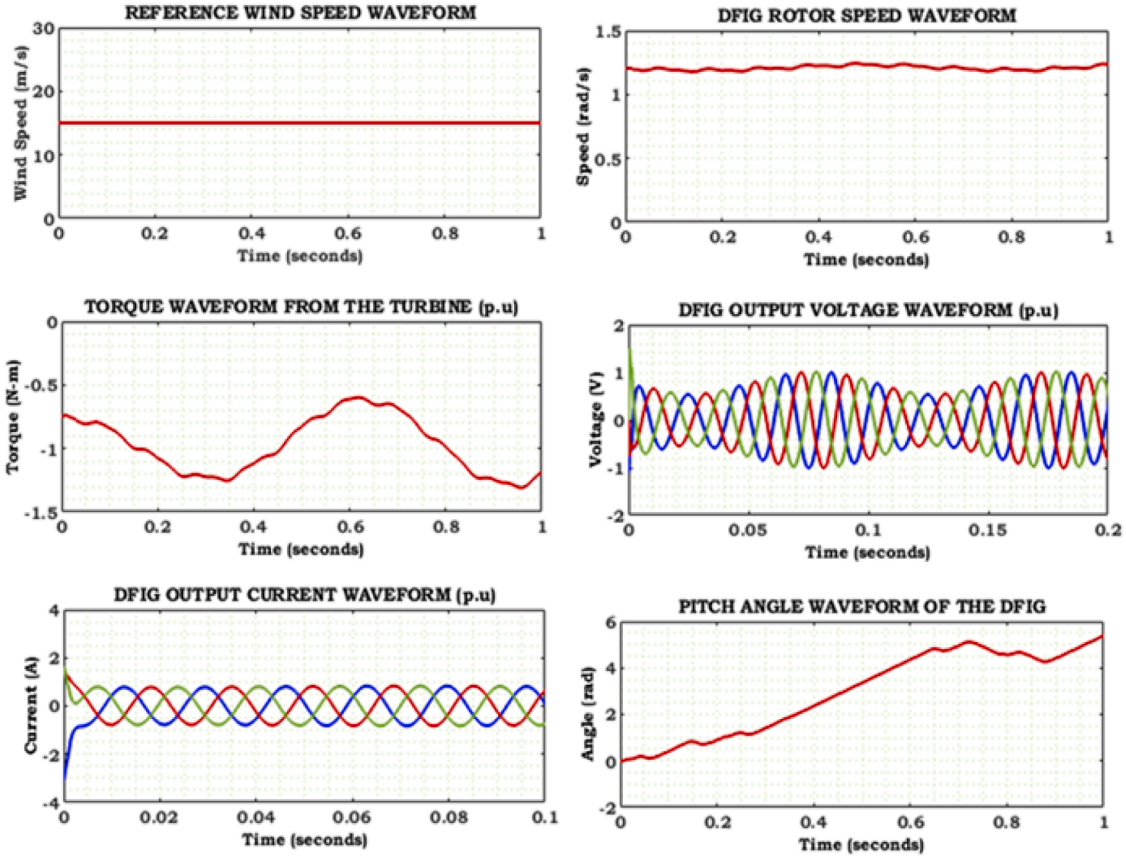


Fig. 13. Wind speed, rotor speed, torque, voltage, current and pitch angle waveforms of DFIG.

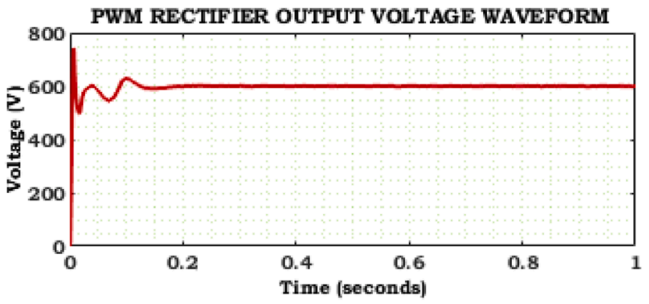


Fig. 14. DC output waveform from PWM rectifier.

$$X_i^{new} = X_i^{old} + D^{new} \cdot N \tag{28}$$

Where, $N \epsilon [0, 1]$ is a normalized nitrogen availability factor acting as a fitness-based gain.In real quokkas, a greater nitrogen value translates into a higher metabolic efficiency, which permits aggressive adaptation towards the best control strategy. The two updating mechanisms work together, and the standard deviation of fitness values in the population is used to constantly govern the transition between exploration and exploitation.

In QSO, dual stopping criteria are adopted for defining the convergence condition. Initially, convergence is attained when the best fitness value denoting the minimum voltage and current tracking error of ANN falls below a predefined threshold. Subsequently, when the maximum number of iterations is reached, convergence is enforced.

The fitness function that evaluates each quokka is derived from the composite time-weighted quadratic error between the reference and actual outputs of the SS-SST over a control horizon T in Eq. (25). Through iterative evaluation and position updating, the QSO algorithm adaptively converges to the optimal ANN parameter set $\{W^*, b^*\}$. Fig. 9 provides the flowchart of QSO algorithm and the specifications of QSO-ANN is provided in Table 1. The ANN inference model then uses these ideal weights when the SS-SST controller is operating in real time. Algorithm 1 denotes the pseudocode of QSO-ANN.

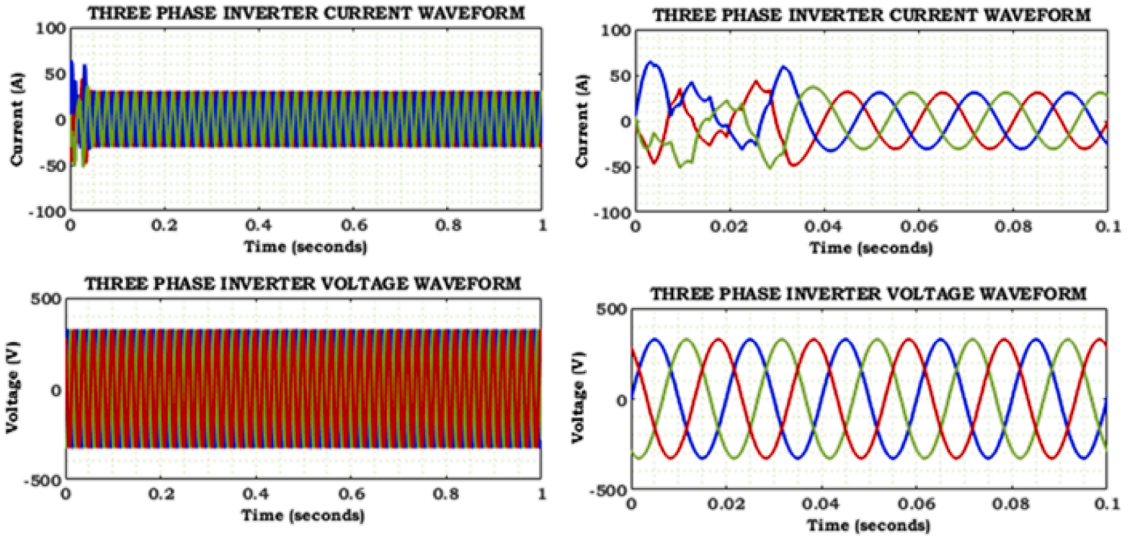


Fig. 15. Current and voltage waveforms of three-phase inverter.

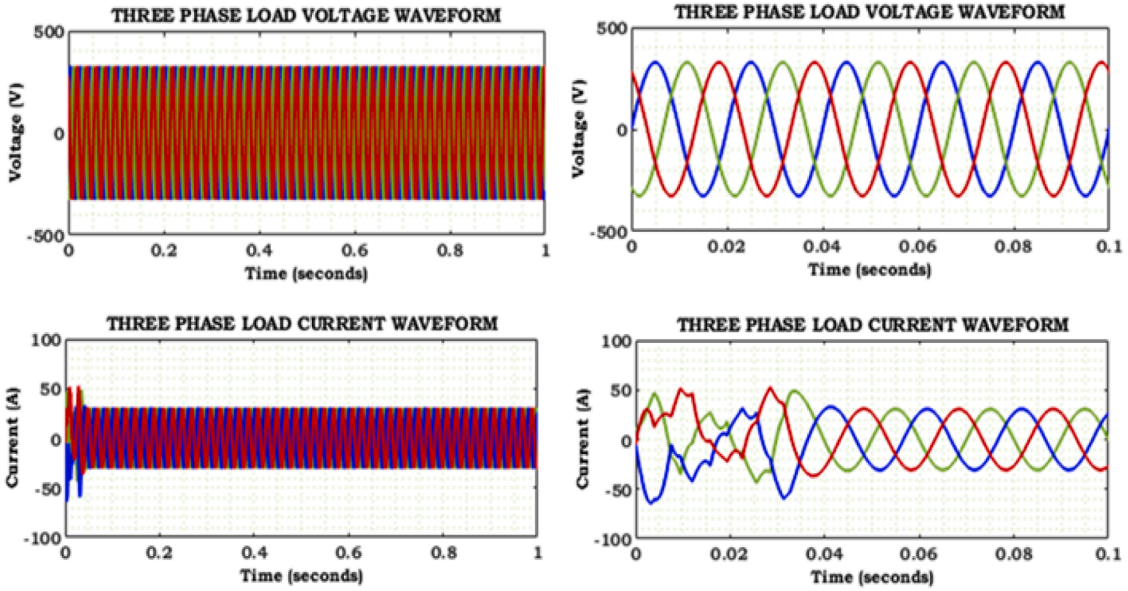


Fig. 16. Three-phase load voltage and current waveforms.

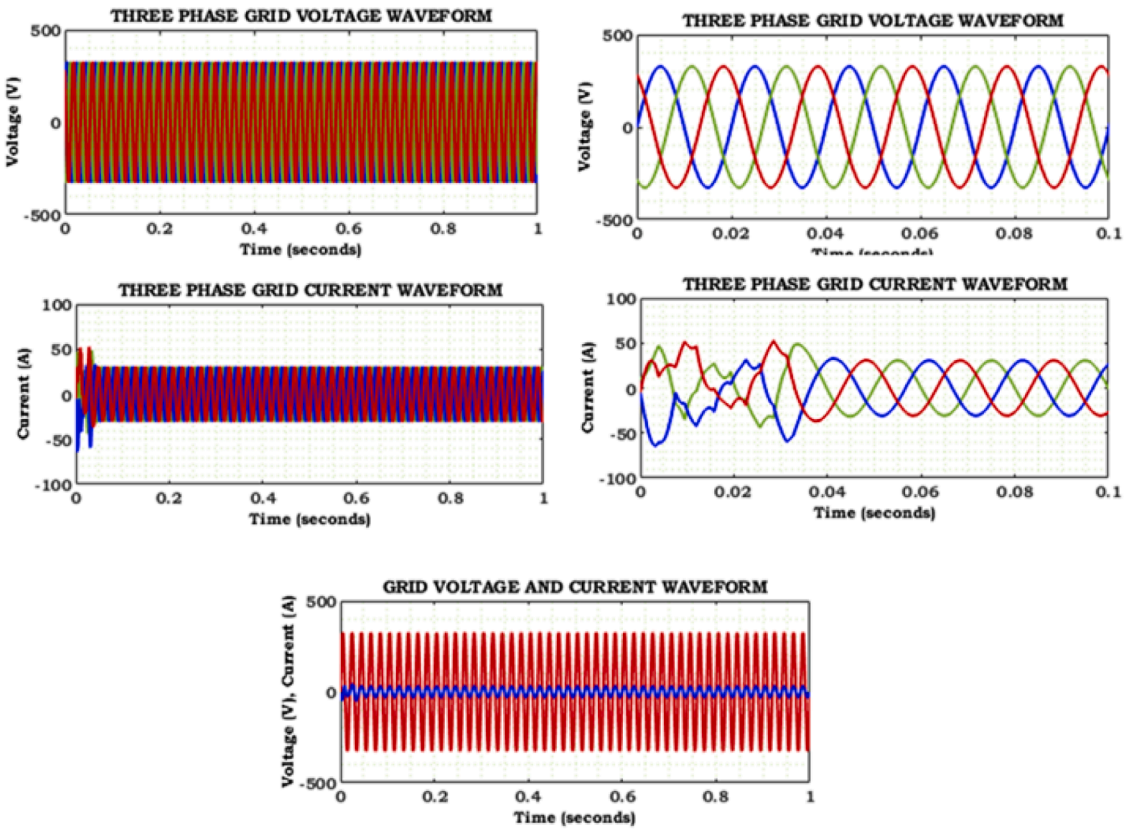


Fig. 17. Steady-state behaviour of grid voltage and current in hybrid system.

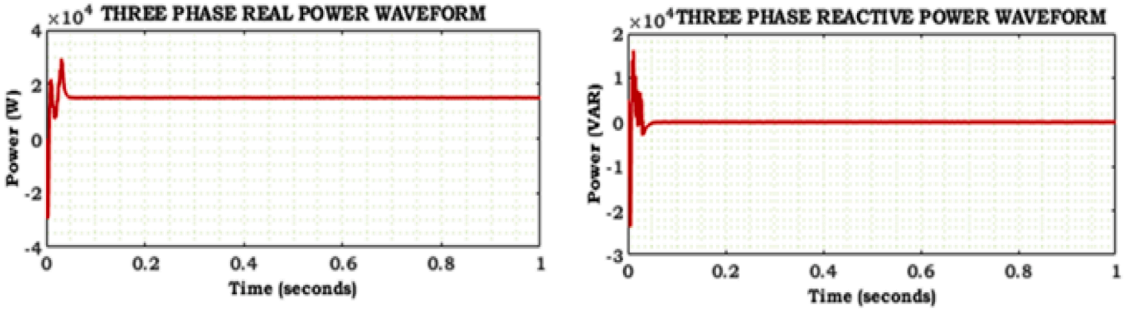


Fig. 18. Time-domain profiles of real and reactive power.

2.6. Stability analysis

The stability of the ANN based controller for SS-SST is assured by the convergence of ANN weights to an optimal region. The bounded error signals $e_v(t),\ \Delta e_v(t), e_i(t), \Delta e_i(t)$ derived from the physically constrained voltage and current measurements are received by ANN. This ensures that the input vector $X(t)$ remains finite under all operating scenarios. The adopting of sigmoid activation function in the hidden layer provides bounded neuron outputs. Subsequently, the linear activation at the output layer restricts the duty cycle $u(t)$ within the permissible range $D \in [0, 1]$ which in turn prevents instability and control saturation of the PWM-driven SS-SST. Considering the control, the ANN acts as a nonlinear state-feedback controller continuously minimizing the quadratic Lyapunov loss function mentioned in Eq. (25). The QSO performs the optimization of ANN weights and biases offline for minimizing the time-averaged current and tracking error. Hence, the closed-loop system operates around a locally asymptotically stable equilibrium in which tracking errors converge toward zero. The parameters of the trained ANN remains fixed and eliminate online weight oscillations facilitating control action. Also, under duty-cycle bounded operation, the SS-SST dynamics are inherently stable against parameter variations with fast recovery. Let the voltage and current tracking errors be defined as,

$$e_v(t) = V_{ref}(t) - V_B(t)$$

$$e_i(t) = I_{ref}(t) - I_B(t)$$

And the error vector is given by,

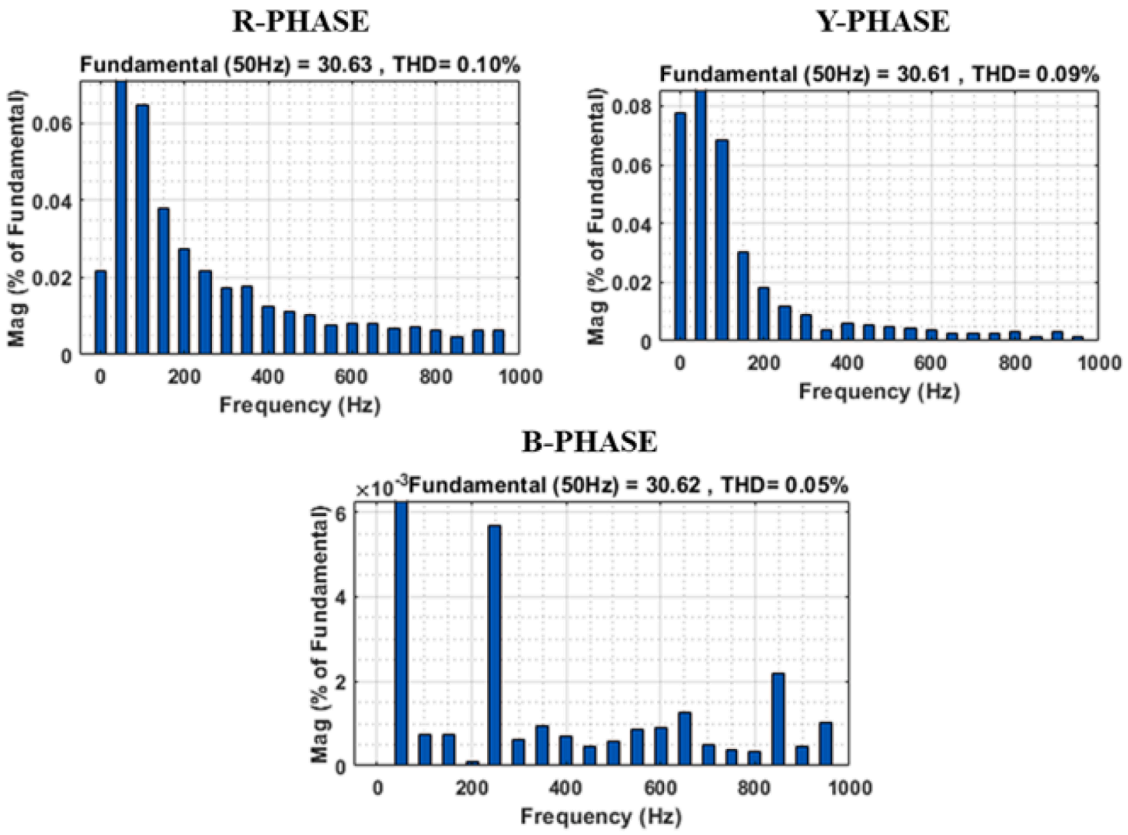


Fig. 19. THD Waveforms.

$$e(t) = \begin{matrix} e_v(t) \\ e_i(t) \end{matrix}$$

The related Lyapunov candidate function is given by,

$$V(t) = \frac{1}{2}\alpha e_v^2(t) + \beta e_i^2(t),\ \alpha > 0,\ \beta > 0 \tag{29}$$

Eq. (29) satisfies $V(t) > 0$ for $(e_v, e_i) \neq 0$ and $V(t) = 0$ at equilibrium. Taking the time derivative,

$$\dot{V}(t) = \alpha e_v \dot{e}_v + \beta e_i \dot{e}_i \tag{30}$$

In compact nonlinear form, the SS-SST closed-loop dynamics is given by,

$$\dot{e}(t) = f(e(t)) + g(e(t))u(t) \tag{31}$$

Here, $f(.)$ and $g(.)$ are bounded nonlinear functions which represent the SS-SST dynamics, $u(t) = f_{ANN}(X(t))$ is the ANN generated duty-cycle command. Since ANN is trained offline using QSO for minimizing the voltage-current tracking error, the controller approximates the ideal nonlinear feedback law $u^*(t)$. Let the ANN approximation error be,

$$\varepsilon(t) = u(t) - u^*(t)$$

With $|\varepsilon(t)| \leq \bar{\varepsilon}$Where, $\bar{\varepsilon}$ represents the maximum approximation error. Assume that around the operating equilibrium $e = 0$, the ideal control law yields exponentially stable error dynamics of the form,

$$\dot{e}(t) = -Ke(t)$$

Where, $K = \begin{matrix} k_v & 0 \\ 0 & k_i \end{matrix}, k_v > 0,\ k_i > 0$

In the presence of ANN approximation error, the actual closed-loop dynamics become,

$$\dot{e}(t) = -Ke(t) + g(e)\varepsilon(t)()$$

Consider the Lyapunov candidate function:

$$V(e) = \frac{1}{2}\alpha e_v^2 + \frac{1}{2}\beta e_i^2$$

With $\alpha > 0,\ \beta > 0$

Clearly, $V(e) > 0,\ \forall e \neq 0$ and $V(0) = 0$

The time derivative of $V(e)$is $\dot{V} = \alpha e_v \dot{e}_v + \beta e_i \dot{e}_i$

Substituting () in above equation, $\dot{V} = -\alpha k_v e_v^2 - \beta k_i e_i^2 + \alpha e_v g_v(e)\varepsilon + \beta e_i g_i(e)\varepsilon$

Assuming that the SS-SST dynamics are bounded such that:

$$|g_v(e)| \leq M_v,\ |g_i(e)| \leq M_i$$

We obtain, $\dot{V} \leq -\alpha k_v e_v^2 - \beta k_i e_i^2 + \alpha M_v |e_v|\bar{\varepsilon} + \beta M_i |e_i|\bar{\varepsilon}$ (.)

Applying Young's inequality, $ab \leq \frac{\delta}{2}a^2 + \frac{1}{2\delta}b^2$,

The cross terms can be bounded as, $\alpha M_v |e_v|\bar{\varepsilon} \leq \frac{\alpha k_v}{2}e_v^2 + \frac{\alpha M_v^2}{2k_v}\bar{\varepsilon}^2$

And $\beta M_i |e_i|\bar{\varepsilon} \leq \frac{\beta k_i}{2}e_i^2 + \frac{\beta M_i^2}{2k_i}\bar{\varepsilon}^2$

Substituting these bounds into (.) gives,

$$\dot{V} \leq -\frac{\alpha k_v}{2}e_v^2 - \frac{\beta k_i}{2}e_i^2 + C\bar{\varepsilon}^2 \tag{37}$$

Where, $C = \frac{\alpha M_v^2}{2k_v} + \frac{\beta M_i^2}{2k_i}$

Eq. (37) shows that when the ANN approximation error is sufficiently small, the negative quadratic terms dominate and $\dot{V} < 0$ outside a small

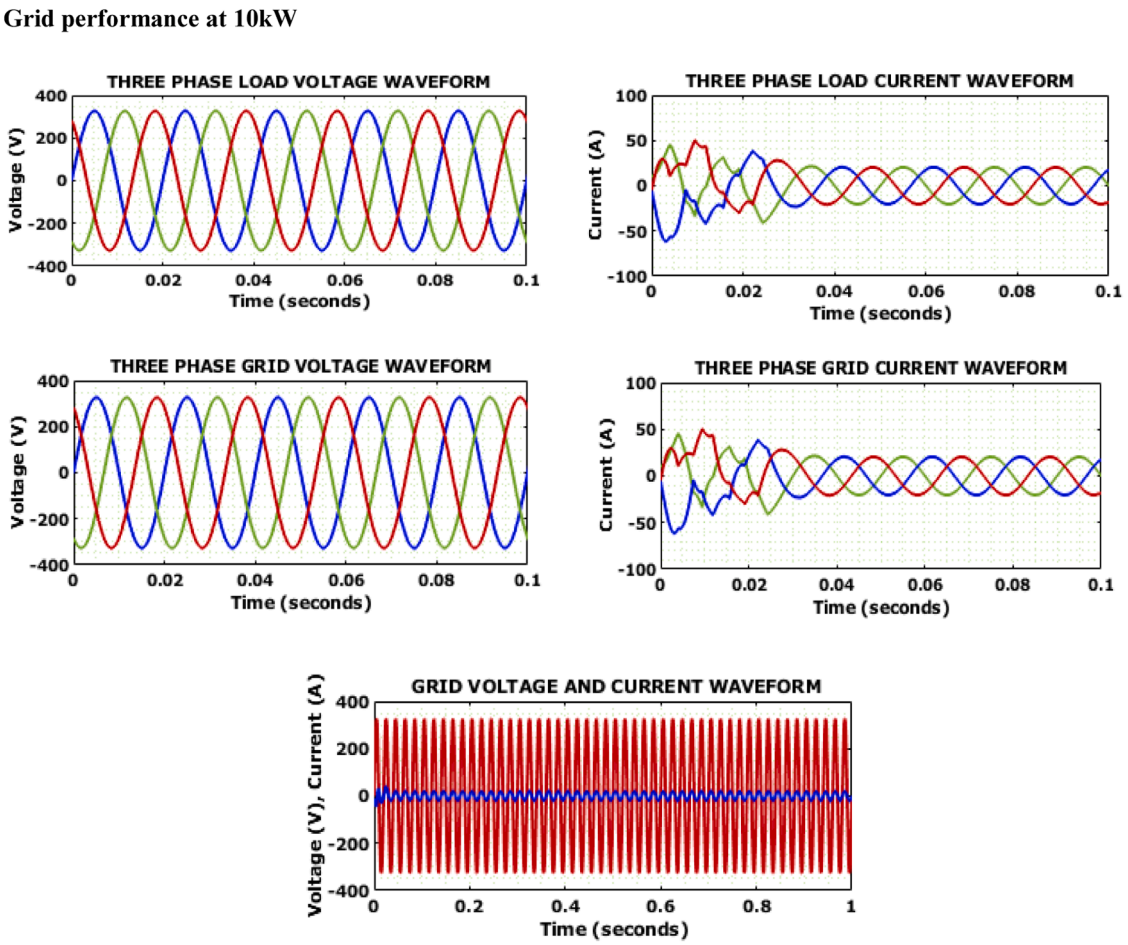


Fig. 20. Load and grid waveforms at 10 kW.

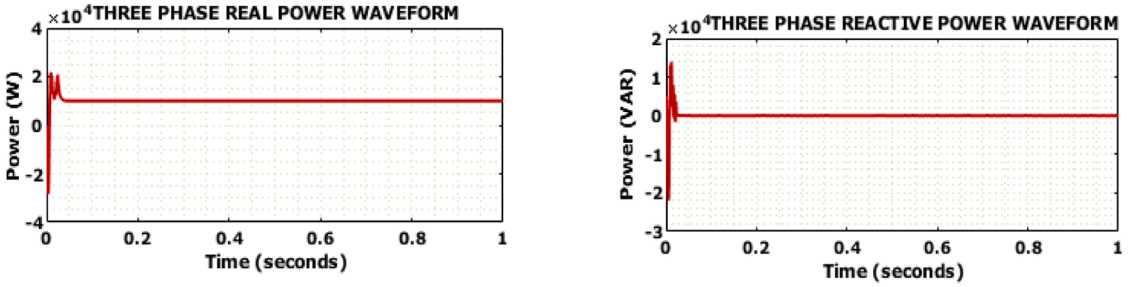


Fig. 21. Real and reactive power waveforms at 10 kW.

neighbourhood of the origin. Consequently, the tracking error vector remains uniformly ultimately bounded. As the ANN training converges and $\bar{\varepsilon}\rightarrow 0$.

Eq. (37) reduces to $\dot{V} = -\frac{\alpha k_v}{2}e_v^2 - \frac{\beta k_i}{2}e_i^2 < 0, \forall e \neq 0$

Thus, the equilibrium point $e = 0$ is locally asymptotically stable according to Lyapunov's direct method, implying convergence of voltage and current tracking errors toward zero.

In addition to improving duty cycle prediction accuracy, this integration of the QSO method with the ANN learning process gives the controller a high degree of flexibility in response to load transients, battery input voltage fluctuations and switching disturbances. In contrast to fixed-gain linear controllers, it lowers overshoot, settling time and steady-state inaccuracy. Additionally, even when the BESS is partially discharged, the closed-loop control system keeps the output voltage and current within strict regulation bands, increasing operational efficiency and extending battery life in microgrid applications that rely on renewable energy.

3. Results and discussion

In-depth MATLAB simulations are conducted under both constant and dynamic operating situations to confirm the efficacy of the suggested QSO-ANN controlled SS-SST in a hybrid renewable microgrid. The PV array, DFIG-based WECS, BESS and grid interface are among the several subsystems for which the results are presented and the corresponding specifications are listed in Table 2. The robustness of the control technique is demonstrated by the analysis of key performance indicators, including rotor dynamics, power stability, State-of-Charge (SoC) management, voltage and current waveforms and harmonic distortion levels.

Grid performance at 15kW

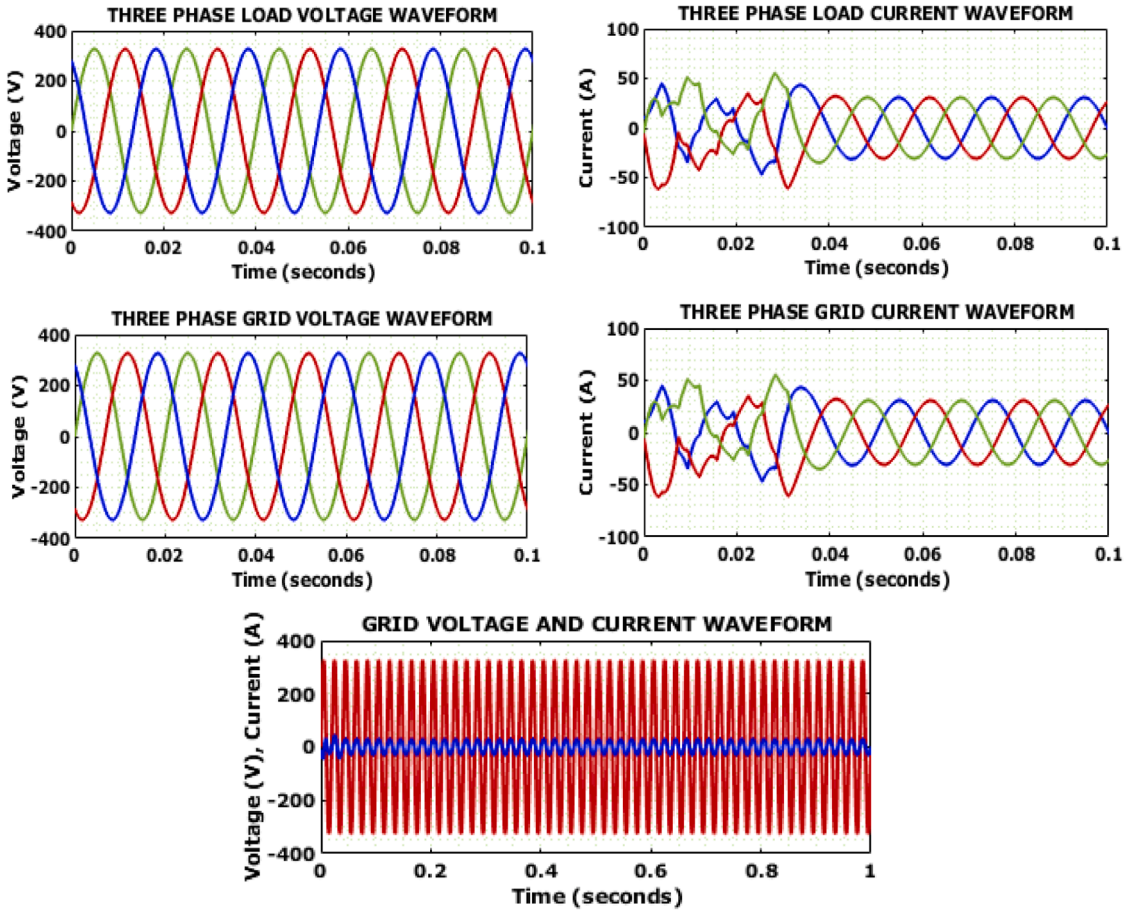


Fig. 22. Load and grid waveforms at 15 kW.

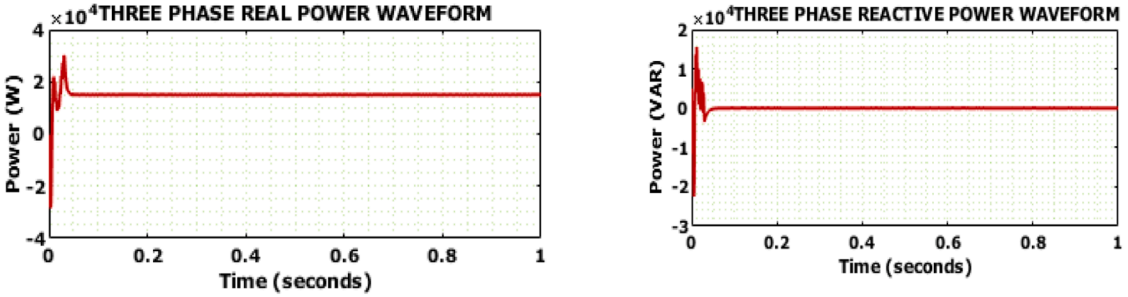


Fig. 23. Real and reactive power waveforms at 15 kW.

The PV system functioning of the microgrid is evaluated under both constant and variable operating conditions and the attained results are provided in Fig. 10 and Fig. 11, respectively. In the first case the temperature and irradiance are maintained at a constant 30°Cand $900W/m^2$, while in the second case, these parameters are varied from25°C to 30°C and $800W/m^2$ to $1000W/m^2$. Under both these conditions, the system is effective in maintaining a stable 600 V.

The battery-side behaviour under QSO-ANN control is displayed in Fig. 12. With little overshoot, the voltage waveform climbs smoothly and rapidly reaches the rated value. After some initial oscillations, the current stabilises, and the SoC stays constant during the operation. These findings demonstrate the extent to which the QSO-ANN controller works in the hybrid microgrid to ensure effective battery management, suppress oscillations and guarantee steady voltage.

The performance of DFIG in WECS with a constant wind input is depicted in Fig. 13. The rotor speed profile is stable as a result of the wind speed staying constant. Aerodynamic dynamics cause slight variations in the turbine torque, but they stay within tolerable operating bounds. The sinusoidal, balanced and grid-compliant waveforms of the DFIG output voltage and current verify proper electromechanical conversion. The turbine controls aerodynamic power capture, as evidenced by the pitch angle response's progressive increase. The stable DC output from the PWM rectifier is provided in Fig. 14. This output is fed to the DC-link of the microgrid.

The three-phase inverter's output voltage and current waveforms are

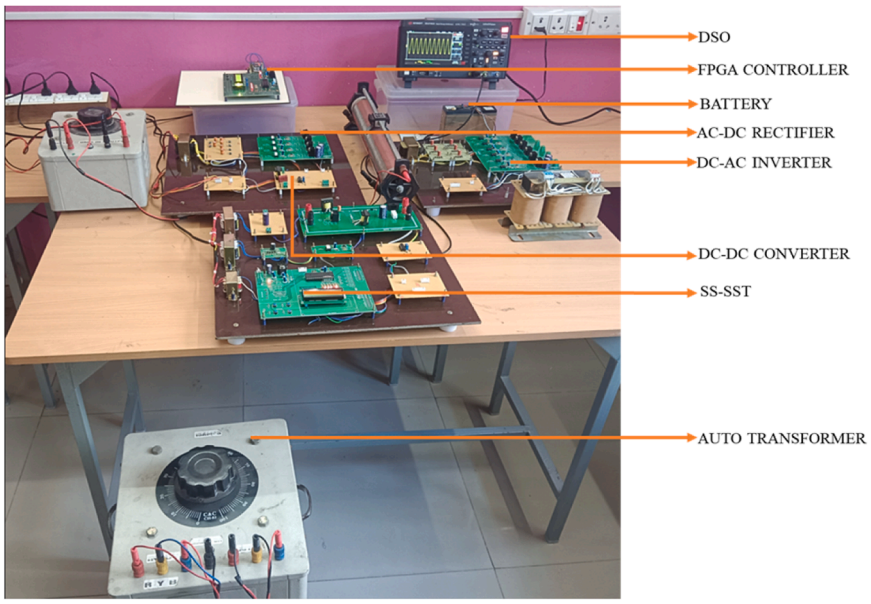


Fig. 24. Laboratory prototype of Hybrid renewable microgrid.

Table 3
Hardware parameter specifications.

Components	Range
Rooftop Solar Panel	10kW
Switch	Semikron IGBT-1200V/10A
Diode	IN4007–1000V/1A
Driver circuit	TLP250–35V/1.5A
Controller	Spartan 6E-3.3.V
Switching frequency	10kHz
Autotransformer	415V/15A
Sampling rate	10–100kHz
Inductor	1mH
Capacitor	100μF

shown in Fig. 15. Effective oscillation damping and stable current management are demonstrated by the current waveforms, which at first exhibit transient oscillations before progressively stabilising into balanced sinusoidal waveforms. The corresponding voltage waveforms show that the inverter generates well-synchronized sinusoidal voltages of similar magnitude following a brief transient interval. The load side voltage and current waveforms illustrated in Fig. 16 show a stable and balanced profile. The grid-side voltage and current responses for the suggested system are shown in Fig. 17. The well-balanced, sinusoidal

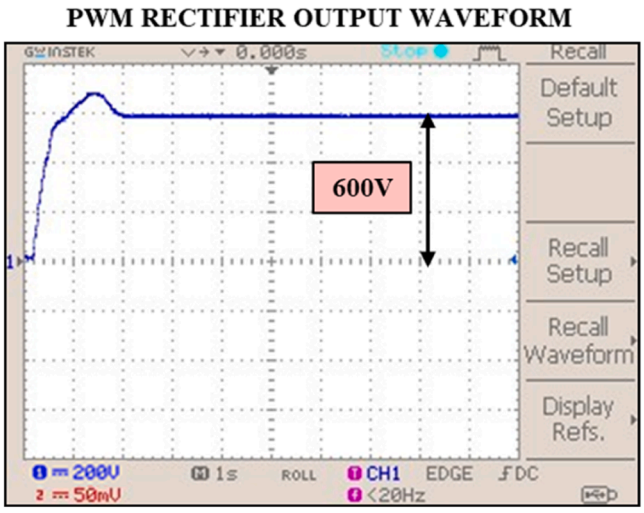


Fig. 26. PWM Rectifier DC output waveform.

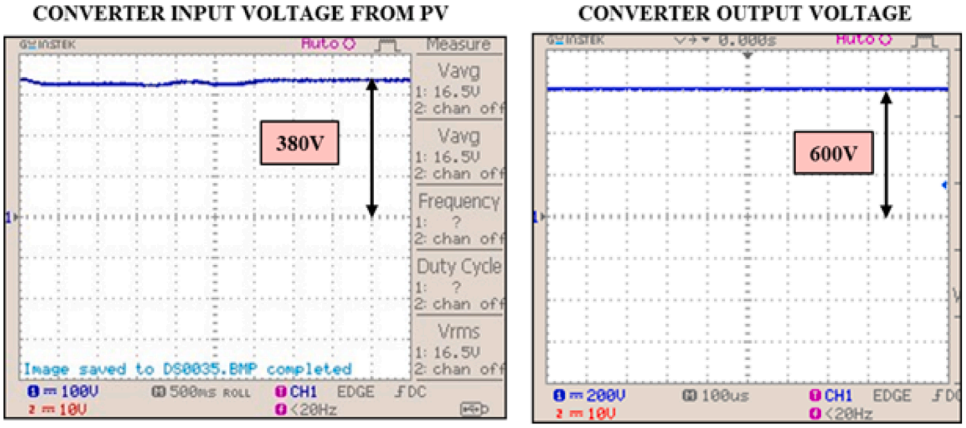


Fig. 25. PV side hardware waveforms.

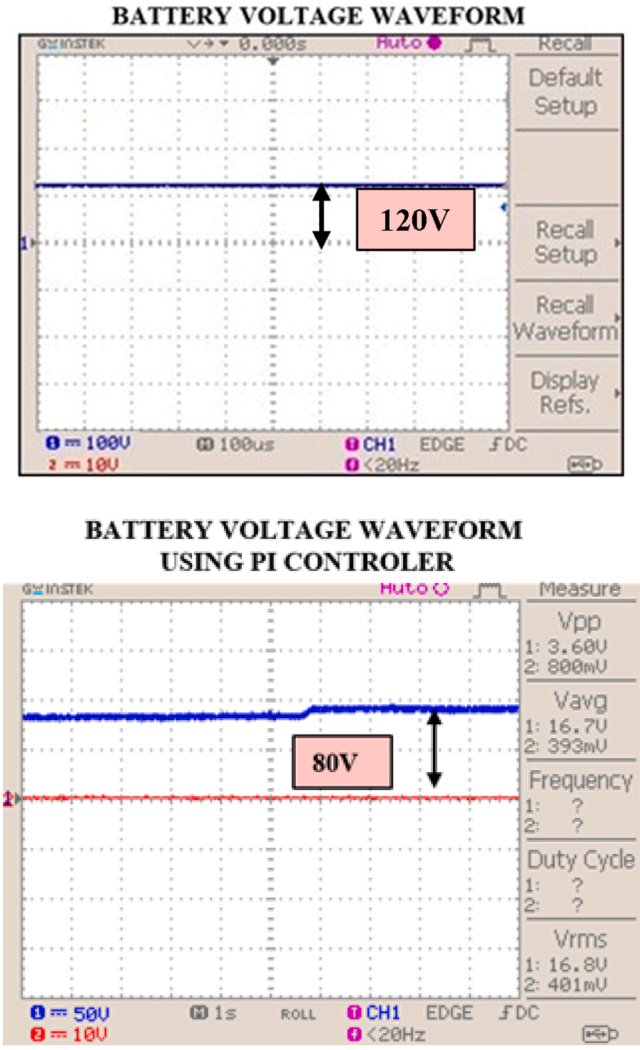


Fig. 27. Battery voltage waveform using QSO-ANN and PI controller.

three-phase voltage and current waveforms verify grid-synchronized operation. The combined voltage-current plot further demonstrates good alignment, indicating near-unity power factor operation.

The three-phase grid-connected system's actual and reactive power waveforms are displayed in Fig. 18. Effective active power transfer to the grid is confirmed when the real power first undergoes a brief transient before swiftly stabilising at a positive constant value. On the other hand, near-unity power factor functioning is indicated by the reactive power, which first shows slight oscillations before settling around zero. These findings show that the system provides consistent active power while reducing the exchange of reactive power, which enhances power quality and guarantees effective microgrid-to-grid integration. Excellent power quality within IEEE standards is confirmed by the THD evaluation in Fig. 19, which displays incredibly low distortion values (0.10% in R-phase, 0.09% in Y-phase and 0.05% in B-phase).

Fig. 20 represents the outcomes of load voltage, load current, grid voltage and grid current along with the in-phase waveforms under 10 kW. Correspondingly, Fig. 21 denotes the attained real and reactive power waveforms. Similarly, Fig. 22 indicates the load and grid outcomes under 15 kW whereas Fig. 23 represents the real and reactive power waveforms at 15 kW. In spite of varying conditions of load a regulated voltage and current outcomes are attained with enhanced reactive power compensation. This proves that the proposed concept is reliable in maintaining enhanced power quality.

3.1. Hardware evaluation

The proposed QSO-ANN controlled SS-SST is validated through a laboratory-scale hardware prototype designed for hybrid renewable microgrid applications. The setup as in Fig. 24, consists of PV input, battery storage, DC-DC converters, an SS-SST stage and grid integration via AC–DC and DC–AC interfaces, all governed by an FPGA controller. A digital storage oscilloscope (DSO) records the system's voltage, current, and power responses under various conditions. The hardware evaluation confirms the simulation outcomes and demonstrates stable high-gain operation, efficient power transfer, low THD and reliable grid synchronization. Table 3 lists out the hardware parameter specification.

The hardware waveform in Fig. 25 illustrates that the converter achieves a smooth voltage boost, converting 380 V input into a regulated 600 V output.

The waveform in Fig. 26 demonstrates that the rectifier quickly regulates the voltage and maintains a constant 600 V output with minimal ripple. Experimental validation results from Fig. 27 demonstrate that the battery voltage remains constant at 120 V, which in turn highlights effective charging and discharging control.

Hardware validation results in Fig. 28 confirm that the grid operates at 230 V, 50 Hz with smooth sinusoidal current injection, thereby ensuring high-quality power delivery.

Results in Fig. 29 indicate that the three-phase system maintains low harmonic distortion, with each phase operating under the acceptable standard threshold.

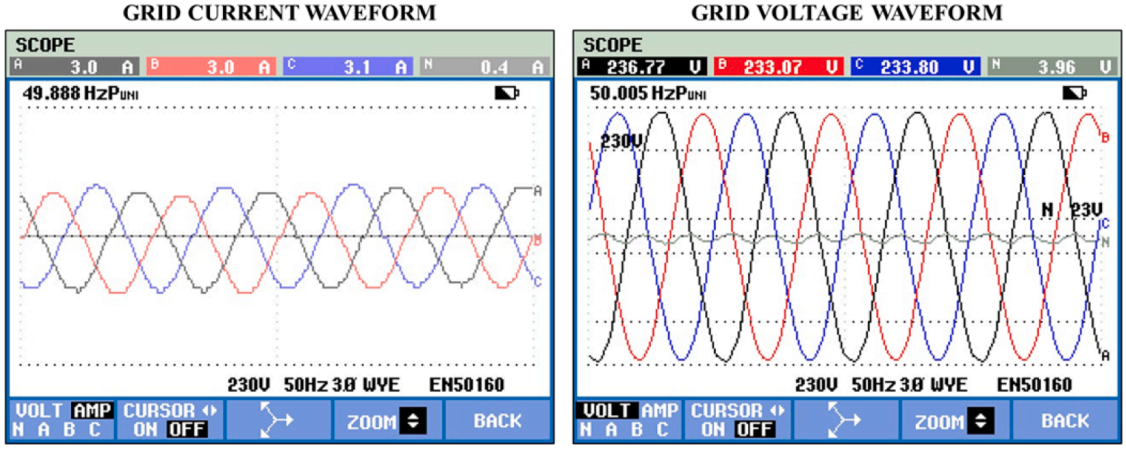


Fig. 28. Grid side characteristic waveforms.

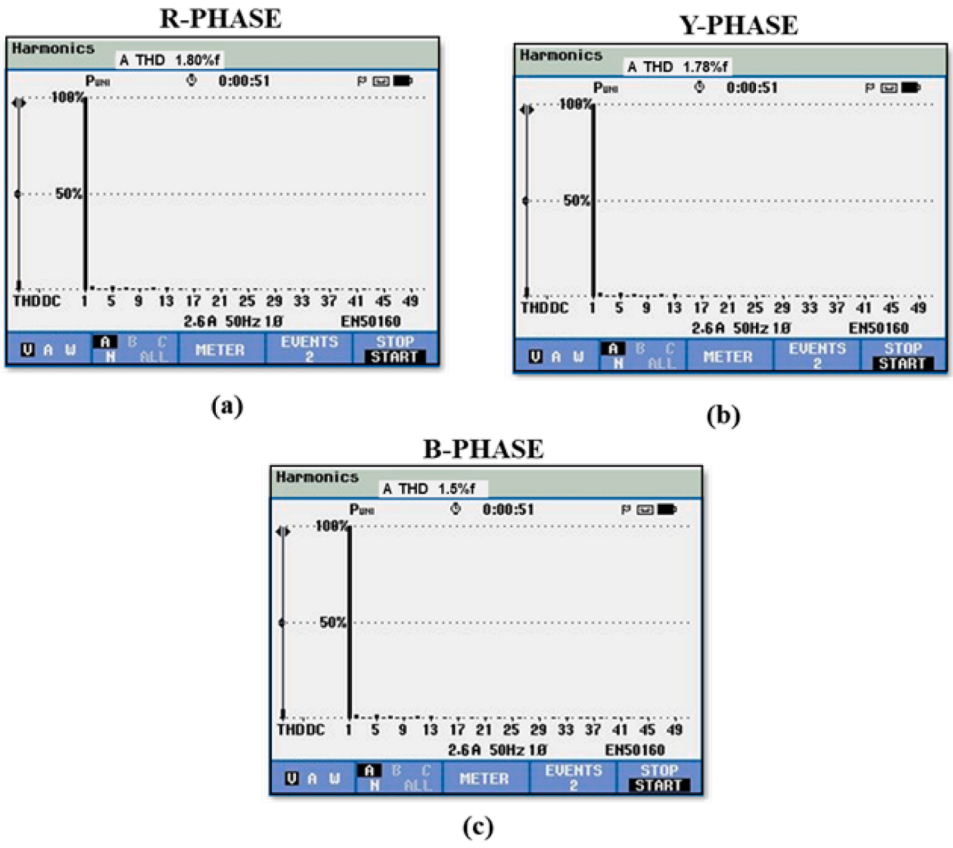


Fig. 29. THD waveforms.

3.2. Comparative evaluation

A comparative evaluation of the results attained in both laboratory and simulation analysis of the SS-SST based renewable microgrid is provided in Table 4. The converter output voltage remains stable and consistent at 600 V in both analyses. Similarly, the battery voltage also remains regulated at 120 V. Grid voltages are maintained at 230 V per phase, with balanced sinusoidal currents that confirm synchronized grid integration at near-unity power factor. THD is observed to be $<0.1\%$ in simulation and between 1.56–1.80% in hardware, both of which satisfy IEEE-519 standards.

sim – simulation, hw – hardware, GA – Genetic Algorithm, PSO – Particle Swarm Optimization

According to Table 5, the suggested QSO-ANN controller outperforms all other approaches in terms of settling time, overshoot, error and THD while retaining high efficiency and power factor close to unity. These comparisons were carried under uniform operating conditions for ensuring fairness. All methods were tested using the same experimental setup, input parameters and environmental conditions. While MPC-based methods are more accurate and stable than conventional controllers, they also carry a greater computational load. Thus, QSO-ANN provides the most sensible and well-rounded approach to SS-SST regulation.

Table 6 shows that advanced controllers outperform classical PI, with ANN and MPCbased schemes improving stability and reducing errors. The testing of the models was carried out under uniform operating conditions. The best results are obtained by QSO-ANN, which offers the maximum gain and phase margins together with the lowest ISE and ITAE, demonstrating its exceptional accuracy and resilience.

Table 4
Comparison of simulation and hardware performance.

Parameter	Simulation Result	Hardware Result
Converter output voltage	600V	600V
Battery voltage	120V	120V
Grid voltage	230V/phase	230V/phase
Grid current	Balanced sinusoidal	Balanced sinusoidal
THD (%)	$< 0.1\%$	$1.5 - 1.8\%$
Power factor	≈ 0.998	≈ 0.99
Efficiency	97%	96%
Settling time (ms)	55ms	60ms
Voltage ripple (%)	0.4%	0.6%
Overshoot (%)	2.5%	3%
Real power (kW)	$\sim 15kW$	$\sim 10kW$
Reactive power (kVAR)	≈ 0.2 kVAR	≈ 0.34kVAR

Table 7 indicates that conventional PI control offers limited robustness, tripping beyond 30% voltage sag and showing slow recovery under same experimental setup, input parameters and environmental conditions. Advanced controllers like ANN, GA-ANN and TV-MPC improve disturbance tolerance significantly. The proposed QSO-ANN achieves the highest robustness, withstanding up to 45% voltage sag, handling frequency deviations within $\pm 0.1Hz$, and ensuring the fastest recovery times, demonstrating its effectiveness in maintaining battery stability and supporting microgrid resilience.

The convergence characteristics of QSO algorithm is plotted in Fig. 30 in terms of iteration number and best fitness value. On observing, it is clear that QSO exhibits faster convergence within less number of

Table 5
Comparative performance analysis of controllers for SS-SST.

Controller	Settling time (ms)	Overshoot (%)	Steady state error (%)	Grid current THD (%)	Power factor	Efficiency (%)	DC-link ripple (%)
PI	120	12	5	3.5	0.96	92.3	1.5
SMC	80	5	2	2.75	0.97	94	1
FLC	95	8	3	2.4	0.98	93.5	1.2
ANN	80	6	2	1.4	0.98	94.3	0.9
GA-ANN	70	4	1.5	1.25	0.98	94.1	0.7
PSO-ANN	60	3	1	1.2	0.98	94.9	0.6
FCS-MPC	65	3	1	1.0	0.99	95	0.5
CCS-MPC	60	3	1	0.9	0.99	95.7	0.5
TV-MPC	58	3	1	0.7	0.99	96	0.5
QSO-ANN	55	2–3	< 1	< 0.1% (sim)	0.998(sim) 0.99(hw)	97(sim) 96(hw)	0.4 (sim) 0.6 (hw)

iterations and further maintains consistently in remaining iterations. When compared to other algorithms like GWO and PSO, QSO is highly suitable for the optimization of real-time control parameters.

Table 8 denotes the comparison of QSO with PSO and GWO under similar experimental conditions. As listed in Table 8, the proposed QSO algorithm provides the best optimization performance, achieving the minimum mean best fitness of 1.2×10^{-15}, reaching convergence in only 18 iterations and requiring the lowest computational time of 31.4 s. This faster convergence and reduced computation time indicate that QSO provides a more effective search mechanism for optimizing ANN weights and biases by achieving higher accuracy with less iteration.

The proposed architecture is highly applicable for real-time implementation due to its reduced complexity and rapid convergence factors. The QSO approach utilizes reduced number of tuning parameters and prevents iterative population explosion thereby aiding in real-time execution on controllers. The ANN allows faster duty-cycle adaption even under fluctuating scenarios and do not demand complex model identification. Considering large-scale integration of PV systems, the scalable and modular characteristics of SS-SST architecture supports expansion towards higher power levels without variations in core control strategy. Added to this, the adaptive QSO-ANN controller assures coordinated sharing of power and grid code compliance maintenance making the proposed work appropriate for large-scale smart grid applications.

Table 6
Stability and performance index comparison of controllers.

Controller	Gain Margin (dB)	Phase Margin (°)	Integral of Squared Error (ISE)	Integral Time Absolute Error (ITAE)
PI	6	30	0.012	0.021
SMC	8	35	0.010	0.018
FLC	9	38	0.009	0.017
ANN	12	50	0.006	0.012
GA-ANN	13	55	0.005	0.010
TV-MPC	14	60	0.0045	0.009
QSO-ANN	15	65	0.004	0.008

4. Conclusion

A HRES microgrid including PV generation, DFIG-based wind system and BESS is designed, modelled and evaluated in this work. As the primary power conversion interface, SS-SST is used to offer higher frequency isolation, lower switching losses and increased dependability over traditional transformer-based systems. In order to overcome the difficulties posed by nonlinear dynamics and variable renewable inputs, the SS-SST interfaced battery is regulated using QSO-ANN controller. Accurate duty cycle generation for efficient voltage and current stabilisation is made possible by the QSO-ANN, which combines the learning capabilities of ANN with the global optimisation capabilities of QSO. The superiority of the suggested controller in attaining quick settling time, less overshoot and less steady-state error while guaranteeing improved power quality is validated by simulation and hardware validation. The results show that QSO-ANN provides the optimum trade-off between dynamic response, efficiency and robustness when compared to conventional PI, SMC, ANN, FLC and advanced MPC-based techniques.

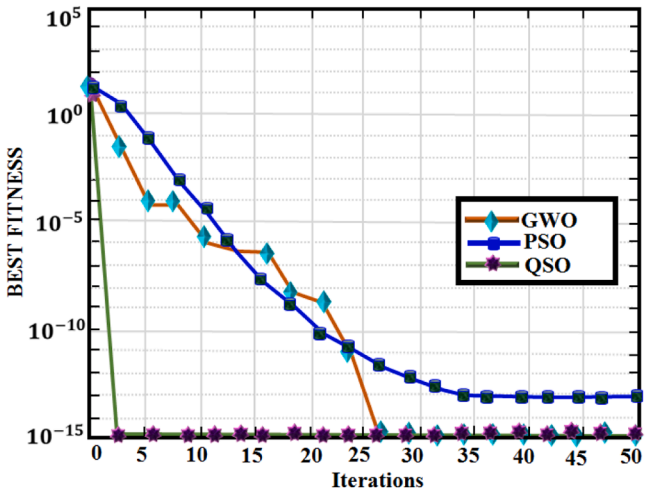


Fig. 30. Convergence characteristics.

Table 7
Robustness evaluation of controllers under disturbances.

Controller	Voltage sag		Frequency deviation		Wind speed	Wind Speed	Irradiance	
	Test condition	V sag (%)	Test condition	Frequency Deviation Handling (Hz)	Disturbance condition	Fluctuation Recovery (ms)	Disturbance condition	Step Change Recovery (ms)
PI	30% voltage reduction for 200 ms	30%	±0.5 *Hz* step deviation	±0.5 *Hz*	Wind speed step change (±20%)	180	Irradiance step change (800–400W/m^2)	200
SMC		35%		±0.3 *Hz*		140		160
ANN		38%		±0.25 *Hz*		110		120
FLC		36%		±0.28 *Hz*		120		130
GA-ANN		40%		±0.2 *Hz*		95		100
TV-MPC		42%		±0.15 *Hz*		85		90
QSO-ANN		45%		±0.1 *Hz*		70		80

Table 8
Quantitative convergence analysis.

Algorithm	Number of runs	Mean Best Fitness	Iterations to convergence	Average computational time (s)
PSO	20	2.8×10^{-12}	34	42.5
GWO	20	1.9×10^{-13}	29	38.7
QSO	20	1.2×10^{-15}	18	31.4

By demonstrating steady DC-link voltage control, dependable battery management, balanced grid-side waveforms, near-unity power factor and THD well within IEEE-519 bounds, the hardware prototype further demonstrates the system's viability. The integration of SS-SST with QSO-ANN control significantly improves microgrid resilience, efficiency and reliability, rendering it a promising solution for next-generation renewable-based distributed energy systems. Although QSO-ANN controller exhibits rapid dynamic response, the quality of training and tuning ranges may affect the performance which in turn requires re-optimization during extreme grid disturbances. Since the ANN controller learns the nonlinear characteristics of the HRES-SST system from available operating scenarios, performance degradation may occur under extreme conditions or unforeseen disturbances that are not sufficiently represented during training. Furthermore, significant changes in system configuration, renewable generation profiles or grid operating conditions may require additional training or retuning of the controller parameters. Future work will focus on developing adaptive and self-tuning mechanisms, incorporating broader operating conditions and extending the proposed approach toward fault-tolerant control and coordinated energy management to improve applicability in large-scale smart grid environments.

Ethics approval

Not applicable.

Consent for publication

Not applicable.

Technical comments

Not applicable.

Funding

The authors received no specific funding for this study.

CRediT authorship contribution statement

Pradeep Ammasaikutti: Writing – original draft, Data curation, Conceptualization. **J Viswanatha Rao:** Writing – review & editing, Validation, Supervision, Project administration, Methodology. **M Gnana Sundari:** Writing – review & editing, Validation, Supervision, Project administration, Methodology. **B Parvathi Sangeetha:** Writing – review & editing, Validation, Supervision, Project administration, Methodology.

Declaration of competing interest

The authors declare that they have no known competing financial interests or personal relationships that could have appeared to influence the work reported in this paper.

Data availability

Data will be made available on request.

References

[1] K.S. Kavin, P. Subha Karuvelam, M. Devesh Raj, M. Sivasubramanian, A novel KSK converter with machine learning MPPT for PV applications, Electr. Power Compon. Syst. (2024) 1–19.
[2] K. Paulsamy, S. Karuvelam, Modeling and design of a grid-tied renewable energy system exploiting re-lift Luo converter and RNN based energy management, Sustainability 17 (1) (2025) 187.
[3] J. Daniel Sathyaraj, R. Arumugam, M. Faustino Adlinde, A novel interleaved Zeta–Cuk converter for microgrid and electric vehicle applications, Electr. Eng. 105 (6) (2023) 4177–4193.
[4] A. Radovanović, J.V. Milanović, Deep learning-based equivalent modelling of hybrid RES plant for efficient, repetitive power system transient stability studies, IEEE Trans. Power. Syst. 39 (2) (2024) 3008–3020.
[5] O. Ayan, B.E. Turkay, Techno-economic comparative analysis of grid-connected and islanded hybrid renewable energy systems in 7 climate regions, Turk. IEEE Access. 11 (2023) 48797–48825.
[6] R. Agarwal, H. Li, Z. Guo, P. Cheetham, The effects of PWM with high dv/dt on partial discharge and lifetime of medium-frequency transformer for medium-voltage (MV) solid State transformer applications, IEEE Trans. Ind. Electron. 70 (4) (2023) 3857–3866.
[7] L. Zheng, R.P. Kandula, D. Divan, Device voltage stress from ground leakage current in medium-voltage solid-State transformer, IEEE Trans. Power. Electron. 38 (1) (2023) 566–577.
[8] A. Cervone, Z. Li, D. Dujic, Modularized diode rectifiers: a new Family of solid-State transformers, IEEE Trans. Power. Electron. 40 (4) (2025) 4747–4751.
[9] K.S. Parihar, M.K. Pathak, Dual mode control scheme for DAB based solid-State transformer, IEEE Trans. Power. Electron. 39 (3) (2024) 3144–3155.
[10] H. Xiao, K. Prasad, J. Kilby, A review of solid-State transformer-based Ultra-fast charging station technologies: topologies, control, and grid interaction, Energies 18 (17) (2025) 4705.
[11] F. Cozac, T.S. Amorim, I. Yahyaoui, D.B. Mendo, L.F. Encarnação, Multifunctional control strategy for a hybrid solid-State transformer applied to modern distribution electric grids, Electronics 13 (20) (2024) 4123.
[12] Z. Li, E. Hsieh, Q. Li, F.C. Lee, High-frequency transformer design with medium-voltage insulation for resonant converter in solid-state transformer, IEEE Trans. Power. Electron. 38 (8) (2023) 9917–9932.
[13] P. Nachankar, H.M. Suryawanshi, P. Chaturvedi, D. Atkar, Fault resilient soft switching DC–DC converter for modular solid state transformer applications, IEEE Trans. Ind. Appl. 58 (2) (2022) 2242–2254.
[14] L.A. Budiwicaksana, D.C. Lee, Submodule capacitor voltage balancing through high-frequency-side control for multiport MMC-based solid-state transformers, IEEE Open J. Ind. Electron. Soc. 5 (2024) 302–316.
[15] R. Cisneros, R. Gao, R. Ortega, I. Husain, A PI+ passivity-based control of a wind energy conversion system enabled with a solid-state transformer, Int. J. Control 94 (9) (2021) 2453–2463.
[16] P. Khemmook, S. Khomfoi, C. Manee-in, The design of the PI controller with SmartCtrl for the Solid State Transformer in the solar farm application, in: 2017 14th International Conference on Electrical Engineering/Electronics, Computer, Telecommunications and Information Technology (ECTI-CON), 2017, pp. 501–504.
[17] T. Liu, X. Yang, W. Chen, Y. Xuan, Y. Li, L. Huang, X. Hao, High-efficiency control strategy for 10-kV/1-MW solid-state transformer in PV application, IEEE Trans. Power. Electron. 35 (11) (2020) 11770–11782.
[18] B.L. Liu, Y.B. Zha, T. Zhang, Sliding mode control of solid state transformer using a three-level hysteresis function, J. Cent. South. Univ. 23 (8) (2016) 2063–2074.
[19] A.F. Nardoto, A.E. Amorim, L.F. Encarnação, W.M. Santos, E.J. Bueno, D. M. Blanco, Model Predictive Control For Solid State Transformer, 223, Electric Power Systems Research, 2023 109658.
[20] Y. Yan, W. Chen, R. Liang, Y. Qi, M. Huang, Z. Zhou, W. Li, Finite control set-model predictive power management of Multi Active bridge converter, IEEE Trans. Aerosp. Electron. Syst. 61 (2025) 16110–16120.
[21] A. Nardoto, A. Amorim, N. Santana, E. Bueno, L. Encarnação, W. Santos, Adaptive model predictive control for DAB converter switching losses reduction, Energies 15 (18) (2022) 6628.
[22] C. Ding, H. Zhang, Y. Chen, G. Pu, Research on control strategy of solid state transformer based on improved MPC method, IEEE Access. 11 (2023) 9431–9440.
[23] Y. Ma, T. Zhang, X. Zhou, Fuzzy-improved linear active disturbance rejection control of solid State transformer inverter stage, in: 2021 IEEE International Conference on Mechatronics and Automation (ICMA), 2021, pp. 600–605.
[24] N. Zemirline, N. Kabeche, S. Moulahoum, Artificial neural network controller for grid current quality improvement in solid-state transformers, J. Power Electron. 24 (5) (2024) 799–809.
[25] Z. Jing, L. Gao, C. Wu, D. Liang, Linear quadratic regulator-based coordinated voltage and power control for flexible distribution networks, Energies 18 (2) (2025) 361.
[26] S. Kamble, P. Chaturvedi, C.J. Chen, V.B. Borghate, Enhancing reliability and efficiency of grid-connected solid-state transformer through fault detection and classification using wavelet transform and artificial neural network, Electr. Eng. 106 (3) (2024) 2525–2535.

[27] N. Zemirline, N. Kabeche, S. Moulahoum, Artificial neural network controller for grid current quality improvement in solid-state transformers, J. Power Electron. 24 (5) (2024) 799–809.
[28] D. Yeddu, B.L. Rao, Application of Solid State Transformer in wireless charging system of EV and voltage profile enhancement by using AI techniques, J. Integr. Sci. Technol. 12 (1) (2024) 705.
[29] A. Karthick, Review on State of charge prediction of battery management system in electric vehicles, in: Proceedings of the Institution of Mechanical Engineers, Part D: Journal of Automobile Engineering, 2025, https://doi.org/10.1177/09544070251380931.
[30] W.J. AL-kubaisy, B. AL-Khateeb, Quokka swarm optimization: a new nature-inspired metaheuristic optimization algorithm, J. Intell. Syst. 33 (1) (2024) 20240051.